

10-16-2014

Simulation of Fracture of Concrete Using Micropolar Peridynamics

Asadollahi Aziz

Follow this and additional works at: https://digitalrepository.unm.edu/ce_etds

Recommended Citation

Aziz, Asadollahi. "Simulation of Fracture of Concrete Using Micropolar Peridynamics." (2014). https://digitalrepository.unm.edu/ce_etds/97

This Thesis is brought to you for free and open access by the Engineering ETDs at UNM Digital Repository. It has been accepted for inclusion in Civil Engineering ETDs by an authorized administrator of UNM Digital Repository. For more information, please contact disc@unm.edu.

Aziz Asadollahi

Candidate

Civil Engineering

Department

This dissertation is approved, and it is acceptable in quality and form for publication:

Approved by the Dissertation Committee:

Dr. Walter H. Gerstle , Chairperson

Dr. Arup K. Maji

Dr. Timothy J. Ross

**SIMULATION OF FRACTURE OF CONCRETE
USING
MICROPOLAR PERIDYNAMICS**

By

AZIZ ASADOLLAHI

**B.Sc., CIVIL ENGINEERING, UNIVERSITY OF TEHRAN, 1998
M.Sc., STRUCTURAL ENGINEERING, UNIVERSITY OF TEHRAN, 2000**

THESIS

Submitted in Partial Fulfillment of the
Requirements for the Degree of

**Master of Science
Civil Engineering**

The University of New Mexico
Albuquerque, New Mexico

July, 2014

© 2014, Aziz Asadollahi

DEDICATION

To my wife and parents

ACKNOWLEDGEMENTS

I would never have been able to finish my thesis without the guidance of my advisor, committee members, help from friends, and support from my family and wife.

I would like to express my deepest gratitude to my advisor, Prof. Walter Gerstle, for his excellent guidance, caring, patience, and providing me with an excellent atmosphere for doing research.

I would also like to thank my committee members, Prof. Arup K. Maji, and Prof. Timothy J. Ross, for serving as my committee members. I also want to thank you for letting my defense be an enjoyable moment.

In addition, thank you to Prof. Jens Lorenz, Prof. Stephen Lau, and Prof. Juan Heinrich for encouraging my studies and their support.

I would like to thank my parents, sisters, and brothers. They were always supporting me and encouraging me with their best wishes.

The most special thanks go to my best partner and friend, my wife. Leila, you gave me your unconditional support and love through all this long process.

Mahshid and Mostafa have been a very dear friends. Thank you for the memorable gatherings, for the endless fun and support at stressful times.

I would like to thank Ron Clipp, who as a good friend has always been a source of energy. Thank you for the chats, the drinks, and for sharing the stress of the last year.

Simulation of Fracture of Concrete Using Micropolar Peridynamics

By

Aziz Asadollahi

B.Sc., Civil Engineering, University of Tehran, 1998

M.Sc., Structural Engineering, University of Tehran, 2000

M.Sc. Civil Engineering, University of New Mexico, 2014

M.Sc., Applied Mathematics, University of New Mexico, 2014

Abstract

The main goal of the thesis is to develop a constitutive damage model for simulating tensile fracture of concrete using the micropolar peridynamics model. Micropolar peridynamics was proposed by Gerstle in 2007 as a generalization to the bond based peridynamics method introduced by Silling in 2000, which was only capable of handling materials with specific Poisson's ratios. Inspired by the bilinear cohesive model in the cohesive crack approach, a new constitutive damage model is proposed to simulate the tensile fracture of a normal-strength concrete. Laboratory experimental data for crack mouth opening displacement vs. load of notched beams, obtained by Chapman in 2011 which are of three different sizes, are used to calibrate the model. It is shown that the simulation results obtained from modeling match very well with those from laboratory experiments, and the size of the fracture process zone, the damage, and cracking patterns are match experiment as well. As a part of the research the isotropicity of the hexagonal particle lattice, proposed by Gerstle in 2011 and used in our simulations, is shown analytically, and the critical time step of the explicit time integration method, which is used to solve the governing equations, is determined.

Table of Contents

List of Figures	X
List of Tables	XIII
Chapter 1 Introduction	1
1.1 Mechanism of tensile fracture of concrete	2
1.2 Bond based peridynamics	6
1.2.1 Basic formulation	7
1.2.2 Numerical approximation and solution to peridynamics equations of motion	8
1.3 Micropolar peridynamic lattice model (MPLM)	9
1.4 Objectives and scope	10
Chapter 2 Formulation of elastic lattice	11
2.1 Isotropicity of hexagonal lattice and rigidity of its members.....	12
2.1.1 Lattice under σ_{xx}	12
2.1.1.1 Young's modulus E_{xx}^{lat}	16
2.1.1.2 Poisson's ratio ν_{xy}^{lat}	17
2.1.2 Lattice under σ_{yy}	17

2.1.2.1 Young's modulus E_{yy}^{lat}	20
2.1.2.2 Poisson's ratio ν_{yx}^{lat}	21
2.1.3 Lattice under pure shear	21
2.1.3.1 Shear modulus G_{xy}^{lat}	25
2.1.4 Isotropy of the hexagonal lattice	25
2.1.5 Axial and flexural rigidity of the lattice members	26
2.1.6 Magnitude of internal forces under σ_{xx} , σ_{yy} , and τ_{xy}	27
2.2 Critical time step	28
2.2.1 Critical time step of a framed structure	32
2.3 2D Co-rotational beam formulation	34
2.3.1 Co-rotational concept	34
2.3.2 Co-rotational formulation	35
Chapter 3 Damage model	38
3.1 Micropolar damage model	38
3.2 Tensile damage index	39
Chapter 4 Calibration of the damage model	43
4.1 Configuration of the beams and material properties of the concrete	43

4.2 Simplification in configuration of beams	44
4.3 Loading specifications	45
4.4 Maximum value of velocity applied to the top particle	46
4.5 Maximum value of the critical Time step	46
4.6 Effect of parameters of damage model on the CMOD-load diagram	47
4.7 Calibration of the damage model for $s = 3.175$ mm	48
4.7.1 Numerical and experimental results for load point displacement	52
4.7. 2 Damage and cracking pattern	56
4.8 Calibration of the damage model for $s = 6.35$ mm	58
4.9 Calibration of the damage model for $s = 12.70$ mm	63
Chapter 5 Conclusions	66
5.1 Future work	68
References	69

List of Figures

Fig. 1.1 Fracture Process zone (Ref. Bazant 2002)	3
Fig. 1.2 Merging micro-cracks to become part of the main crack (Ref. Shah et al. 1995)	3
Fig. 1.3 Mode I Crack for Fictitious crack approach (Ref. et al. Shah 1995).....	4
Fig. 1.4 Stress vs. crack opening displacement curve	4
Fig. 2.1 The concrete plate, blue rectangle, is discretized to hexagonal particles which are interacting by micro-polar links (black links)	12
Fig. 2.2 Horizontally loaded hexagonal lattice	13
Fig. 2.3 Upper segment of section a-a, the horizontal internal loads applied to the Inclined members have not been shown in this figure	14
Fig. 2.4 Internal loading applied to the periodic part of the lattice under σ_{xx}	14
Fig. 2.5 Hexagonal lattice under vertical stress	17
Fig. 2.6 Segment of the lattice located to the right of section $b - b$, the vertical loads applied to inclined members have not been shown in this figure	18
Fig. 2.7 Internal loading applied to the periodic part of the lattice under σ_{yy}	19
Fig. 2.8 The lattice under pure shear.....	21
Fig. 2.9 Internal loading applied to the periodic part of the lattice under pure shear.....	22
Fig. 2.10 Equivalent lattice unit of the lattice loaded in pure shear	23

Fig. 2.11 Simplified lattice unit of the lattice loaded in pure shear	24
Fig. 2.12 Lattice unit under σ_{xx}	27
Fig. 2.13 Lattice unit under σ_{yy}	27
Fig. 2.14 Lattice unit under τ_{xy}	28
Fig. 2.15 Typical fictitious beam	33
Fig. 2.16 Initial and current configuration of a typical fictitious beam	35
Fig. 2.17 Current deformed configuration of a fictitious beam	36
Fig. 3.1 Bilinear softening model used to define the damage index	40
Fig. 4.1 Configuration of the beam specimens	43
Fig. 4.2 Overhangs are replaced with equivalent moment	44
Fig. 4.3 Computational model of D3, lattice spacing, s , is 3.175 mm	45
Fig. 4.4 Typical CMOD-load diagram	47
Fig. 4.5 Numerical and Experimental results for CMOD- Load of D3 beam, $s = 3.175$ mm	49
Fig. 4.6 Numerical and experimental results for CMOD-load of D6 beam, $s = 3.175$ mm	50
Fig. 4.7 Numerical and experimental results for CMOD-load of D9 beam, $s = 3.175$ mm	51

Fig. 4.8 Numerical and experimental results for LPD-load of D3 beam, s = 3.175 mm	53
Fig. 4.9 Numerical and experimental results for LPD-load of D6 beam, s = 3.175 mm.....	54
Fig. 4.10 Numerical and experimental results for LPD-load of D9 beam, s = 3.175 mm	55
Fig. 4.11 Damage pattern of D3 beam for different values of CMOD, see Fig. 4.5 for corresponding load values, s = 3.175 mm	57
Fig. 4.12 Numerical and experimental results for CMOD-load of D3 beam, s = 6.7 mm	59
Fig. 4.13 Numerical and experimental results for CMOD-load of D6 beam, s = 6.35 mm	60
Fig. 4.14 Numerical and experimental results for CMOD-load of D9 beam, s = 6.35 mm	61
Fig. 4.15 Damage pattern of D6 beam for different values of CMOD, see Fig. 4.6 for corresponding load values, s = 6.35 mm	62
Fig. 4.16 Numerical and experimental results for CMOD-load of D9 beam, s = 12.7 mm	64
Fig. 4.17 Damage pattern of D9 beam for different values of CMOD, see Fig. 4.7 for corresponding load values, s = 12.7 mm	65

List of Tables

Table 4.1	Nominal beam dimensions in mm	43
Table 4.2	The value of damage model parameters for $s = 3.175$ mm	48
Table 4.3	The color of the damaged fictitious beam based on the range of damage.....	56
Table 4.4	The value of damage model parameters for $s = 6.35$ mm.....	58
Table 4.5	The value of damage model parameters for $s = 12.7$ mm.....	63

Chapter 1 Introduction

Concrete is an important material which is dominant in construction all over the world. However, due to the lack of knowledge, technology, and budget for full scale load testing of structures and monitoring the response of its components under a complex loading, most of the relations given in the design codes are based on the outputs obtained from simplified laboratory experiments. To compensate for the effect of these simplifications, the values of the safety factors are increased, which does not necessarily mean gaining extra safety. In addition, lots of other simplifications are made to make the design of structures by engineers easier. For example, most modern design codes neglect the tensile strength of concrete completely. These all mean wasting money, and making it difficult for engineers to see and understand the real behavior of structures.

On the other hand, significant progress in the power of computers in the recent years can be beneficial in performing more realistic simulations. To this end, developing simple and effective constitutive material models is essential to allow engineers safely use the full capacity of structural components, and to design more economical, and safer structures. Micropolar peridynamics is a simple, powerful approach which has been developed to simulate ultimate behavior of structures by considering all kind of failure mechanisms. This method needs an appropriate material constitutive model to simulate realistic response of structures. Since the goal of this research is to develop a constitutive material model for micropolar peridynamics to simulate the tensile fracture, the method will be presented after introducing tensile fracture mechanism of the concrete and some other computational methods which have been developed to simulate tensile fracture of concrete during the past years.

1.1 Tensile fracture mechanism of concrete

Concrete is a two-phase material consisting of the matrix and aggregate bonded together at the interface. The matrix and aggregate are very different in modulus of elasticity, thermal coefficient, and response to the change of moisture content, and the interfacial transition zone between the matrix and the aggregate has more voids and is weaker compared to the bulk cement matrix. Furthermore, hardening of fresh concrete is accomplished by a loss of moisture in the cement paste, which causes shrinkage of the concrete, which happens only in the cement paste. During the shrinkage tensile stress can be developed in some parts of the concrete which may cause shrinkage cracks before loading. Concrete's tensile strength is about 8 to 15 percent of its compressive strength. Since concrete is a heterogeneous material, as stated before it has very complicated fracture mechanisms, which are related to its microstructure. During fracture, the high stress state near the crack tip causes micro-cracking at flaws. These flaws result from water-filled pores, air voids acquired during casting, and shrinkage cracks due to curing process. The inelastic zone around the crack tip consisting of micro-cracks as shown in Fig. 1.1 is called fracture process zone (FPZ). The fracture process zone is the intermediate space between the cracked and the uncracked portion. It has been observed that micro-cracks have random orientation with respect to the main crack plane, and their density decreases with increasing distance from the surface of the main crack. As the crack propagates these micro-cracks merge and become a single structure to give continuity to the already existing crack (Fig. 1.2) [Shah et al. 1995].

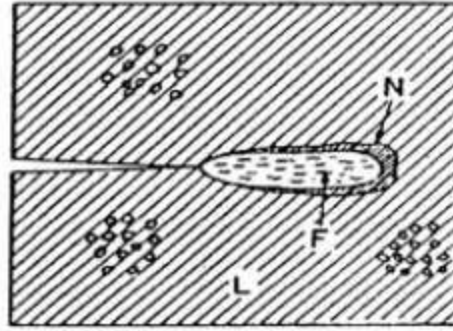


Fig. 1.1 Fracture process zone (Ref. Bazant 2002)

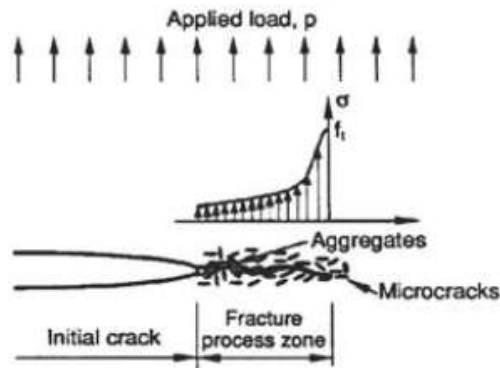


Fig. 1.2 Merging micro-cracks to become part of the main crack (Ref. Shah et al. 1995)

Due to the presence of the large FPZ in concrete, classical linear elastic fracture mechanics is inadequate to model this material. Extensive studies has be conducted to develop a method to simulate fracture of concrete, and a major advance in this field was made by Hillerborg in 1976 [Hillerborg et al. 1976]. Inspired by the models proposed to simulate the fracture of ductile materials, Hillerborg proposed the fictitious crack model. In this method fracture formation is regarded as a gradual phenomenon in which the separation of the surfaces involving in the crack takes place across an extended crack tip,

also called “fictitious crack” or “cohesive zone” as shown in Fig. 1.3, and is resisted by cohesive tractions.

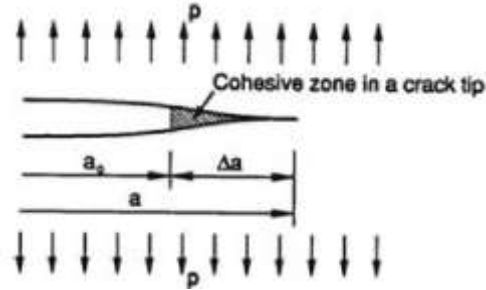


Fig. 1.3 Mode I crack for fictitious crack approach (Ref. Shah et al. 1995)

As the surfaces (known as cohesive surfaces) separate, the traction first increases until a maximum is reached as shown in Fig. 1.4, and then subsequently reduces to zero, which results in complete separation.

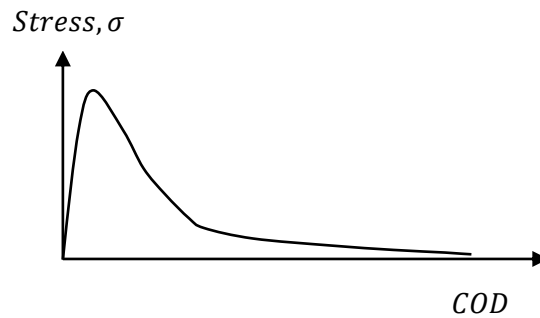


Fig. 1.4 Stress vs. crack opening displacement curve

The cohesive crack model was used in finite element methods to simulate the fracture of concrete. The notable ones among numerous finite element methods are:

fictitious crack approach, discrete crack approach, and smeared crack approach. One problem with these methods is that they use meshing to discretize the domain and, therefore, to simulate crack propagation and stress concentration at the crack tip they require re-meshing, which is very difficult. In addition, they need a criterion for specifying the crack direction, a criterion for failure, and other criteria for crack initiation and crack propagation. The dependency of the results on mesh refinement is the major deficiency with smeared crack models [Nguyen and Chun 2005].

The lattice modeling technique is another approach which has received considerable attention in recent years for modelling the fracture of heterogeneous media such as concrete. A lattice model discretizes a continuum by axial elements capable of transferring forces and moments. The earliest model was proposed by Hrennikoff in 1941 [Hrennikoff 1941] but the method languished due to insufficient computing power. Hansen and coworkers developed a model for simulating fracture of metals using a square lattice of frame elements [Hansen et al. 1989]. Bazant [Bazant et al. 1990], and Schlangen and Van Mier [Schlangen and Van Mier 1992] demonstrated frame and truss lattice models for modeling concrete, primarily at the meso-structural (material) level. They used a triangular lattice network, because it was found to better simulate the heterogeneous structure of concrete.

To obtain a realistic pattern for crack patterns, the lattice model were modified in order to distinguish between the hardened cement paste, the fine and coarse aggregates, and a bond layer between the cement paste and aggregate constituents. In all of these lattice-type models, the focus was on the elastic truss or frame elements, connected at nodes and these elements were simply eliminated when the maximum tensile stress in an

element reached a critical value. Arslan [Arsalan et al. 2002] has simulated concrete beams by regarding the matrix phase as elastic and tension softening. Ince [Ince 2005] included the inherent disorder in the microstructure by assigning random strength and/or stiffness properties to the elements in a regular lattice.

Silling [Silling 2000] introduced the peridynamics method. This method does not have the drawbacks of finite element methods and lattice methods. Since this method is the base for the method that has been used in this research, it will be presented in greater detail.

The peridynamic theory is based on integral equations, in contrast with the classical theory of continuum mechanics, which is based on partial differential equations. Since partial derivatives do not exist on crack surfaces and other singularities, the classical equations of continuum mechanics cannot be applied directly when such features are present in a deformation. The integral equations of the peridynamic theory can be applied directly, because they do not require partial derivatives [Silling 2000].

The ability to apply the same equations directly at all points in a mathematical model of a deforming structure helps the peridynamic method avoid requiring special techniques of fracture mechanics. For instance, in peridynamics, there is no need for a separate crack growth law based on a stress intensity factor.

1.2 Bond based peridynamics

The essence of this method is that integration, rather than differentiation, is used to compute the force on a material particle. The method falls into the category of nonlocal models, because particles separated by a finite distance can interact with each other.

1.2.1 Basic formulation

Suppose a body occupies a reference configuration in a region \mathfrak{R} . It is assumed that each pair of particles interact through a vector-valued function \mathbf{f} such that the force per unit reference volume due to interaction with other particles denoted by \mathbf{L} is obtained from the following equation:

$$\mathbf{L}(\mathbf{x}, t) = \int_{\mathfrak{R}} \mathbf{f}(\mathbf{u}(\mathbf{x}', t) - \mathbf{u}(\mathbf{x}, t), \mathbf{x}' - \mathbf{x}) dV_{x'}, \quad (1.1)$$

here $\mathbf{u}(\mathbf{x}, t)$ is the displacement of the particle located at point \mathbf{x} at time t , and $\mathbf{L}(\mathbf{x}, t)$ is the resultant force applied to the particle of unit volume at point \mathbf{x} by the other particles of the body surrounding this particle. Knowing the value of forces applied to the particle at \mathbf{x} and the body force applied to this particle, Newton's second law for this particle implies that:

$$\rho \ddot{\mathbf{u}} = \mathbf{L}(\mathbf{x}, t) + \mathbf{b}. \quad (1.2)$$

It is also assumed that the force that two particles apply to each other have the same magnitude but opposite sense. These forces are assumed to be parallel to the relative current position vector of particles. Another assumption is that if the distance between two particles is greater than a number which is called the horizon of the material and denoted by δ , then the particles do not interact or apply force to each other. The adequacy of this method relies on defining appropriate force function \mathbf{f} such that the main features of the material under study is attained in the simulations.

1.2.2 Numerical approximation and solution to peridynamic equations of motion

To solve Eq. 1.2 numerically, the body is discretized into particles, each with a known volume in the reference configuration. Taken together, the particles form a grid. Then the following approximations are used. First it is assumed that each particle's mass is concentrated at its centroid, and the particles interact through their centroids, regardless of their size. So the integral in Eq. 1.1 is simplified to the following finite sum:

$$L(\mathbf{x}_i, t) = \sum_p \mathbf{f}((\mathbf{u}_p - \mathbf{u}_i), (\mathbf{x}_p - \mathbf{x}_i)) \Delta V_p, \quad (1.3)$$

where i is the index of the particle under consideration and p is the index of the other particles which are in the material horizon of the particle i . Vector \mathbf{x}_i is the position vector of the centroid of the particle i .

To obtain the current values of displacement, velocity, and acceleration, the following time integration is usually used. Acceleration of any particle is obtained by using the applied force to the particle:

$$\ddot{\mathbf{u}}(t) = \frac{\mathbf{F}(t)}{m}. \quad (1.4)$$

The forward Euler integration method is used to obtain the value of velocity at time $t + \Delta t$:

$$\dot{\mathbf{u}}(t + \Delta t) = \dot{\mathbf{u}}(t) + \ddot{\mathbf{u}}(t)\Delta t, \quad (1.5)$$

and the backward Euler integration method is used to obtain the value of displacement:

$$\mathbf{u}(t + \Delta t) = \mathbf{u}(t) + \dot{\mathbf{u}}(t + \Delta t)\Delta t. \quad (1.6)$$

Once the value of velocities and displacements of the particles are updated, the force applied to the particles is obtained and the process is repeated to determine the response of the structure at the next time step. Since explicit time integration is used, the value of time step needs to be limited to critical time step which will be determined in the next chapter.

One of the drawbacks of bond-based peridynamics is that it restricts Poisson's ratio of the material to 1/3 in 2D problems and 1/4 in 3D. To overcome this limitation, the micropolar peridynamics was proposed by Gerstle in 2007 [Gerstle et al. 2007].

1.3 Micropolar peridynamic lattice model (MPLM)

In this method it is assumed that, in addition to force, particles apply moments to each other. This means that each particle is sensitive to the rotation of the surrounding particles, and if a particle rotates, the other particles will apply moment to that particle to resist deformation.

With the material mass represented by particles in a lattice, Newton's 2nd law of motion is applied to each particle i :

$$\sum_{j=1}^{N_i} \mathbf{F}_{ij} + \mathbf{F}_{exti} = \Delta m \ddot{\mathbf{u}}_i, \quad (1.7)$$

$$\sum_{j=1}^{N_i} \mathbf{M}_{ij} + \mathbf{M}_{exti} = \Delta I \ddot{\boldsymbol{\theta}}_i, \quad (1.8)$$

where \mathbf{F}_{ij} and \mathbf{M}_{ij} are the force and moment vectors, respectively, exerted by particle j on particle i , \mathbf{F}_{exti} and \mathbf{M}_{exti} are the externally applied force and moment vectors, respectively, applied to the centroid of particle i , $\ddot{\mathbf{u}}_i$ and $\ddot{\boldsymbol{\theta}}_i$ are the linear and angular acceleration vectors, respectively, of the centroid of particle i , Δm and ΔI are the mass

and mass momentum of particles respectively, and N_i is the number of particles, j , that are in the neighborhood (“material horizon, δ ”) of particle i . The vector functions \mathbf{F}_{ij} and \mathbf{M}_{ij} describe the internal forces and moments between neighboring lattice particles, and from these functions, the material and fracture behaviors emerge. In the bond-based damage model, the functions \mathbf{F}_{ij} and \mathbf{M}_{ij} also depend upon evolving damage parameters, ω_{ij} which will be defined on the chapter three, associated with the “link” between particle i and particle j .

To decrease the computational cost, it is assumed that the lattice is hexagonal, which is discussed in more detail in the next chapter. In 2D, each particle is spaced a distance, s , from its six nearest neighbors. Also it is assumed that material horizon is $1.5s$ so that each particle can interact only with at most six surrounding particles.

As an aid to obtain the forces and moments between particles, it is assumed that each particle is connected to the surrounding particles by fictitious elastic beams forming a triangular lattice. In the next chapter a new method is used to show the isotropicity of the lattice, and obtain the axial and flexural rigidity of the fictitious beams.

1.4 Objectives and scope

In chapter two first we demonstrate the isotropicity of the hexagonal lattice under plain stress. Rahman [Rahman 2012] has shown this numerically, and we show it analytically. Then we obtain the critical time step of the explicit time integration method that is implemented in PDQ; PDQ is a software developed by Prof. Gerstle, Prof. Atlas, professor in the Department of Physics & Astronomy at UNM, and their graduate

students. Finally, we present co-rotational formulation to include large displacements in our simulations.

In chapter three we introduce a new damage model for micropolar peridynamics to simulate tensile fracture of concrete. Using this damage model, it is possible to obtain results which are in good agreement with experimental data.

In chapter four we calibrate the damage model we introduced in chapter three by using the available experimental results. For this, we use the results of experiments which was conducted on notched beams by Chapman [Chapman 2011]. Finally we present the conclusions and suggestions in chapter five.

Chapter 2 Formulation of elastic lattice

In section 2.1 first we simulate a concrete plate of thickness " t " by a hexagonal lattice and investigate its isotropicity, and then we determine the axial and flexural rigidity of the lattice members, considered as elastic beams. In section 2.2 we determine the critical time step of the explicit time integration method used in the simulations, and finally in section 2.3 we present the 2D co-rotational formulation of beams.

2.1 Isotropicity of hexagonal lattice and rigidity of its members

In this section, a solid plate is modeled as a hexagonal lattice, as shown in Fig. 2.1, and the periodic nature of the hexagonal lattice is used to obtain the internal forces under uniaxial tension and pure shear. Then the axial and flexural rigidity of the lattice are determined. Moreover, by using obtained Young modulus and Poisson's ratio of the lattice, its isotropicity is demonstrated.

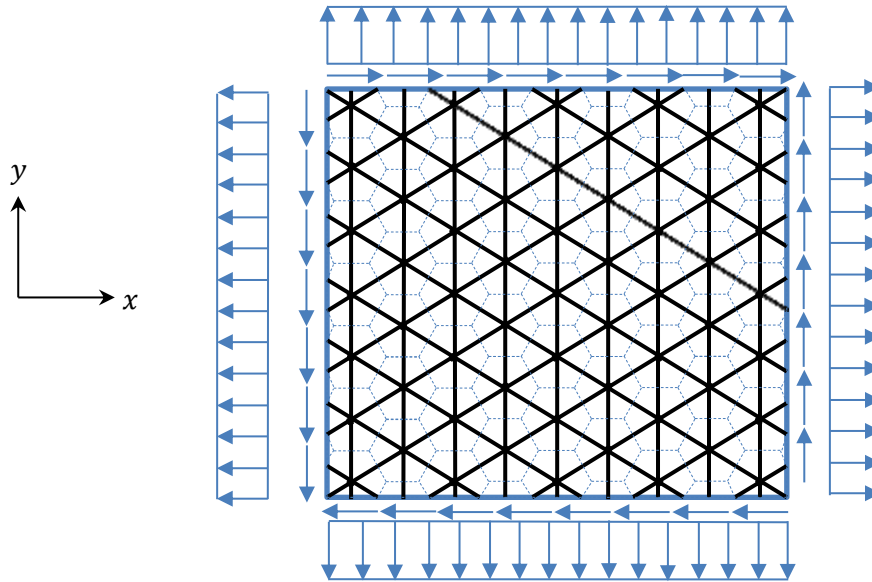


Fig. 2.1 The concrete plate, blue rectangle, is discretized to hexagonal particles which are interacting by micro-polar links (black links)

2.1.1 Lattice under σ_{xx}

Suppose a hexagonal lattice which is under a uniform horizontal normal stress σ_{xx} as depicted in Fig. 2.2. We assume that all of the elements have axial rigidity EA , flexural rigidity EI , and length s . Another assumption for this lattice is that the number of elements is large enough to assume translational symmetry and hence conclude that the nodes cannot rotate under this loading. Therefore, the inflection point of the lattice members is located at their midpoints.

Due to the contraction of lattice in y direction under this loading, the vertical members will be under compression. Cutting lattice using imaginary section $a - a$ and considering the equilibrium of the upper segment, the relation between internal vertical loads applied to the midpoint of inclined and vertical members can be determined.

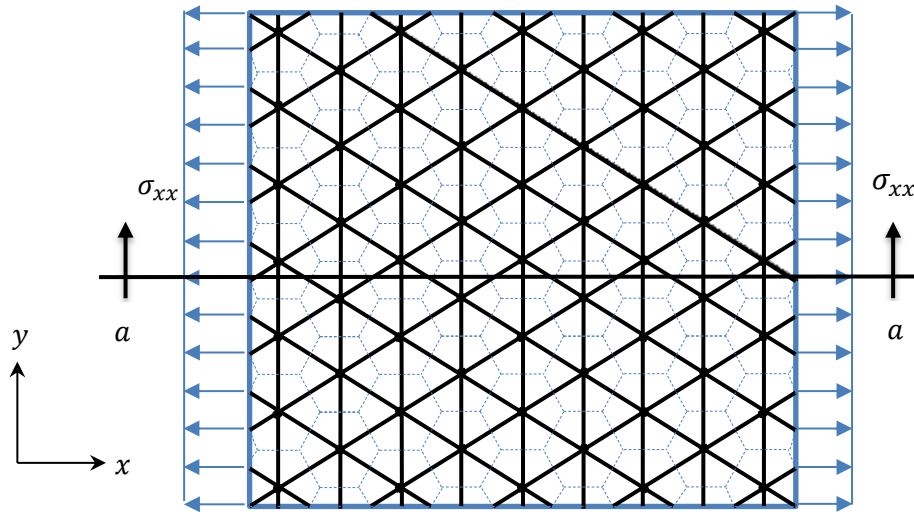


Fig. 2.2 Horizontally loaded hexagonal lattice

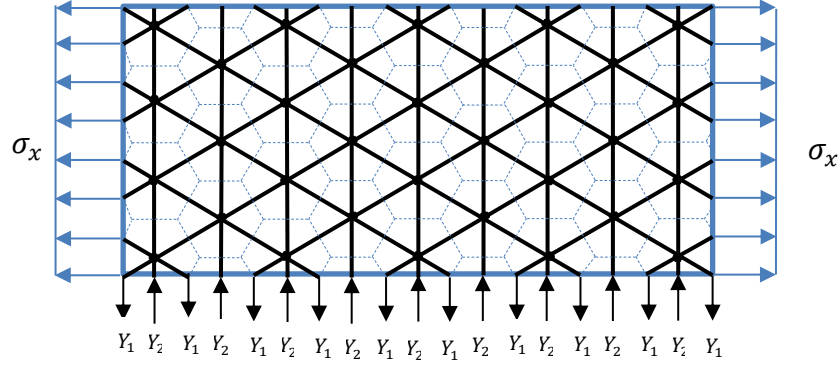


Fig. 2.3 Upper segment of section a-a, the horizontal internal loads applied to the Inclined members have not been shown in this figure.

Consideration of equilibrium of the segment shown in Fig. 2.3 in y direction gives:

$$\sum F_y = 0; \quad Y_1 - Y_2 = 0; \quad Y_1 = Y_2 =: Y. \quad (2.1)$$

Therefore, considering translational symmetry in both x and y directions, the periodic part of the lattice, the part which is trapped inside the hexagonal particles in the figures above, has to be loaded as depicted in Fig. 2.4:

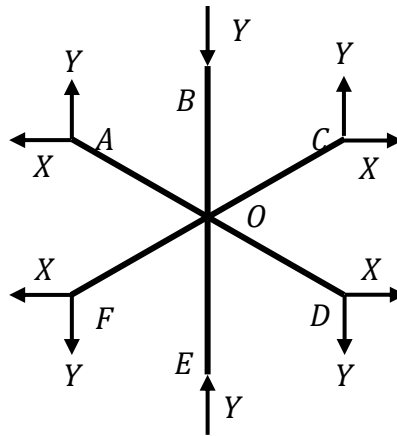


Fig. 2.4 Internal loading applied to the periodic part of the lattice under σ_{xx}

Assuming that the lattice is under plane stress, the magnitude of the horizontal loads is determined based on the contribution of each inclined member in resisting the applied uniform stress:

$$X = \frac{st}{2} \sigma_{xx}. \quad (2.2)$$

The magnitudes of the vertical loads are obtained using uniformity of strain in the y direction, equality of vertical strain of imaginary line AF and member BE in Fig. 2.4. To determine the vertical normal strain of imaginary line, first relative displacement of points A and F in y direction needs to be obtained by using the virtual work method:

$$\delta_y^{A/F} = 2 \left(\frac{\frac{\sqrt{3}s}{4} \cdot \frac{\sqrt{3}s}{4} \cdot \frac{s}{2}}{3EI} X + \frac{\frac{\sqrt{3}s}{4} \cdot \frac{s}{4} \cdot \frac{s}{2}}{3EI} Y - \frac{\frac{1}{2} \cdot \frac{1}{2} \cdot \frac{s}{2}}{EA} X - \frac{\frac{1}{2} \cdot \frac{\sqrt{3}}{2} \cdot \frac{s}{2}}{EA} Y \right), \quad (2.3)$$

where $\delta_y^{A/F}$ denotes displacement of A relative to F in the y direction. Thus, vertical strain of AF is:

$$\varepsilon_{yy}^{A/F} = \frac{\delta_y^{A/F}}{l_{AF}} = -\frac{Xs^2}{8EI} + \frac{\sqrt{3}Ys^2}{24EI} - \frac{X}{2EA} - \frac{\sqrt{3}Y}{2EA}. \quad (2.4)$$

The vertical strain of BE is:

$$\delta_y^{BE} = \frac{Ys}{EA}, \quad \varepsilon_{yy}^{BE} = \frac{\delta_y^{BE}}{l_{BE}} = \frac{Y}{EA}. \quad (2.5)$$

The uniformity of strain in y direction, gives ($\varepsilon_{yy}^{BE} = \varepsilon_{yy}^{A/F}$):

$$\frac{Y}{EA} = -\frac{Xs^2}{8EI} + \frac{\sqrt{3}Ys^2}{24EI} - \frac{X}{2EA} - \frac{\sqrt{3}Y}{2EA}. \quad (2.6)$$

Using Eq. 2.6, Y is determined:

$$Y = \frac{\sqrt{3}(s^2EA - 12EI)}{3(s^2EA + 12EI)} X. \quad (2.7)$$

Having the magnitude of X , given in Eq. 2.2, the magnitude of Y is obtained:

$$Y = \frac{\sqrt{3}st(s^2EA - 12EI)}{6(s^2EA + 12EI)} \sigma_{xx}. \quad (2.8)$$

2.1.1.1 Young's modulus E_{xx}^{lat}

Now, the relationship between horizontal strain and stress is determined, and it is used to obtain Young's modulus in x direction:

$$\delta_x^{A/C} = 2 \left(\frac{\frac{s}{4} \cdot \frac{s}{4} \cdot \frac{s}{2}}{3EI} X - \frac{\frac{\sqrt{3}s}{4} \cdot \frac{s}{4} \cdot \frac{s}{2}}{3EI} Y + \frac{\frac{\sqrt{3}}{2} \cdot \frac{\sqrt{3}}{2} \cdot \frac{s}{2}}{EA} X + \frac{\frac{1}{2} \cdot \frac{\sqrt{3}}{2} \cdot \frac{s}{2}}{EA} Y \right) \quad (2.9)$$

Therefore, the vertical strain of the imaginary line connecting A to C is:

$$\varepsilon_{xx}^{A/C} = \frac{\delta_x^{A/C}}{l_{AC}} = \frac{\sqrt{3}s^2}{72EI} - \frac{Ys^2}{24EI} + \frac{\sqrt{3}X}{2EA} + \frac{Y}{2EA}. \quad (2.10)$$

The values of X and Y in equations 2.2 and 2.8 are plugged in Eq. 2.10 to obtain the value of ε_{xx}^{AC} :

$$\varepsilon_{xx} = \varepsilon_{xx}^{A/C} = \frac{\sqrt{3}st(s^2EA + 4EI)}{2EA(s^2EA + 12EI)} \sigma_{xx}. \quad (2.11)$$

Hence, the Young's modulus in the x direction is:

$$E_{xx}^{lat} = \frac{\sigma_{xx}}{\varepsilon_{xx}} = \frac{\sqrt{3}EA(s^2EA + 12EI)}{6st(s^2EA + 4EI)} . \quad (2.12)$$

2.1.1.2 Poisson's ratio ν_{xy}^{lat}

The obtained strains in x and y directions are used to determine the Poisson's ratio, ν_{xy}^{lat} , of the lattice:

$$\nu_{xy}^{lat} = \left| \frac{\varepsilon_{yy}}{\varepsilon_{xx}} \right| = \frac{s^2EA - 12EI}{3(s^2EA + 4EI)} . \quad (2.13)$$

2.1.2 Lattice under σ_{yy}

Consider the vertically loaded lattice depicted in Fig. 2.5:

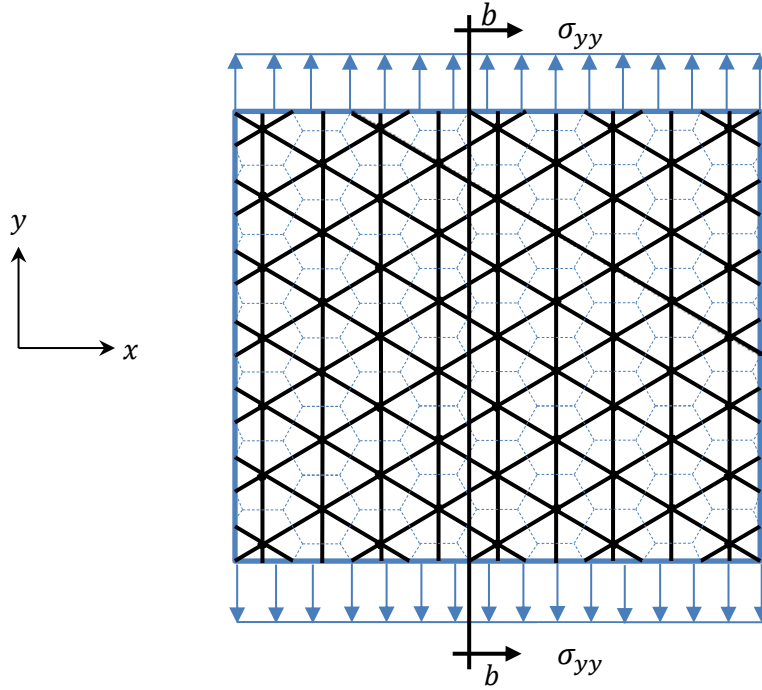


Fig. 2.5 Hexagonal lattice under vertical stress

Again the inflection points are in the midpoint of members. To obtain the horizontal loads applied to the midpoint of inclined members, the equilibrium of horizontal forces applied to the segment located to the right of section $b - b$ which passes through the midpoint of inclined members is considered:

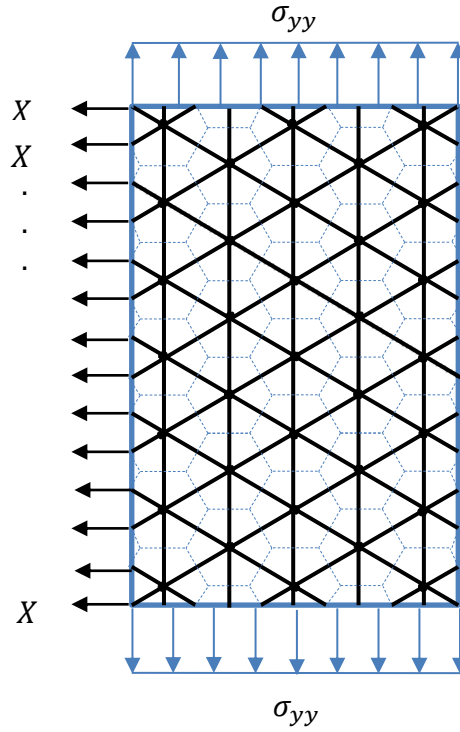


Fig. 2.6 Segment of the lattice located to the right of section $b - b$, the vertical loads applied to inclined members have not been shown in this figure

Equilibrium of the horizontal forces in the figure above gives:

$$\sum F_x = 0; \quad X = 0. \quad (2.14)$$

Since the vertical members are only under axial loads, the lattice unit is only under vertical loads, as shown in Fig. 2.7.

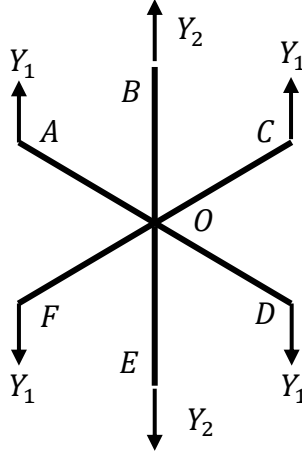


Fig. 2.7 Internal loading applied to the periodic part of the lattice under σ_{yy}

Equilibrium of applied loads to the lattice unit in the y direction gives:

$$Y_1 + Y_2 = \frac{\sqrt{3}}{2} s \sigma_{yy}. \quad (2.15)$$

Because the stress in y direction is uniform, the strains of imaginary line AF and the member BE in y direction must be equal. The strain of AF is:

$$\delta_y^{A/F} = 2 \left(\frac{\frac{\sqrt{3}s}{4} \cdot \frac{\sqrt{3}s}{4} \cdot \frac{s}{2}}{3EI} + \frac{\frac{1}{2} \cdot \frac{1}{2} \cdot \frac{s}{2}}{EA} \right) Y_1, \quad (2.16)$$

$$\varepsilon_{yy}^{AF} = \frac{\delta_y^{A/F}}{l_{AF}} = \left(\frac{s^2}{8EI} + \frac{1}{2EA} \right) Y_1, \quad (2.17)$$

and the strain of BE is:

$$\delta_y^{B/E} = \frac{Y_2 s}{EA}, \quad \varepsilon_{yy}^{BE} = \frac{\delta_y^{B/E}}{l_{BE}} = \frac{Y_2}{EA}. \quad (2.18)$$

Since the obtained strains are equal, we have:

$$\varepsilon_{yy}^{AF} = \varepsilon_{yy}^{BE} ; \frac{Y_2}{EA} = \left(\frac{s^2}{8EI} + \frac{1}{2EA} \right) Y_1, \quad (2.19)$$

Solving equations 2.15 and 2.19, the magnitudes of Y_1 and Y_2 are obtained:

$$Y_1 = \left(\frac{4\sqrt{3}EI}{s^2EA + 12EI} \right) st\sigma_{yy}, \quad (2.20)$$

$$Y_2 = \frac{\sqrt{3}}{2} \left(\frac{s^2EA + 4EI}{s^2EA + 12EI} \right) st\sigma_{yy}. \quad (2.21)$$

2.1.2.1 Young's modulus E_{yy}^{lat}

In this part, the strain in the y direction is obtained in terms of σ_{yy} , and it is used to determine the Young's modulus of the lattice in this direction:

$$\varepsilon_{yy} = \varepsilon_{yy}^{BE} = \frac{Y_2}{EA}, \quad (2.22)$$

$$\varepsilon_{yy} = \frac{\sqrt{3}}{2EA} \left(\frac{s^2EA + 4EI}{s^2EA + 12EI} \right) st\sigma_{yy} = \frac{\sigma_{yy}}{E_{yy}^{lat}}. \quad (2.23)$$

Thus, the Young's modulus in the y direction is:

$$E_{yy}^{lat} = \frac{\sqrt{3}EA(s^2EA + 12EI)}{6st(s^2EA + 4EI)}. \quad (2.24)$$

2.1.2.2 Poisson's ratio ν_{yx}^{lat}

To obtain the Poisson's ratio, first we obtain the lateral strain caused by vertical loading:

$$\delta_x^{AC} = 2 \left(\frac{\frac{\sqrt{3}s}{4} \cdot \frac{s}{4} \cdot \frac{s}{2}}{3EI} - \frac{\frac{\sqrt{3}}{2} \cdot \frac{1}{2} \cdot \frac{s}{2}}{EA} \right) Y_1, \quad (2.25)$$

$$\varepsilon_{xx} = \frac{\delta_x^{AC}}{l_{AC}} = \left(\frac{s^2}{8EI} + \frac{1}{2EA} \right) Y_1. \quad (2.26)$$

Hence, the Poisson's ration is:

$$v_{yx}^{lat} = \left| \frac{\varepsilon_{xx}}{\varepsilon_{yy}} \right| = \frac{s^2 EA - 12EI}{3(s^2 EA + 4EI)}. \quad (2.27)$$

2.1.3 Lattice under pure shear

Consider the hexagonal lattice that is under pure shear as shown in Fig. 2.8.

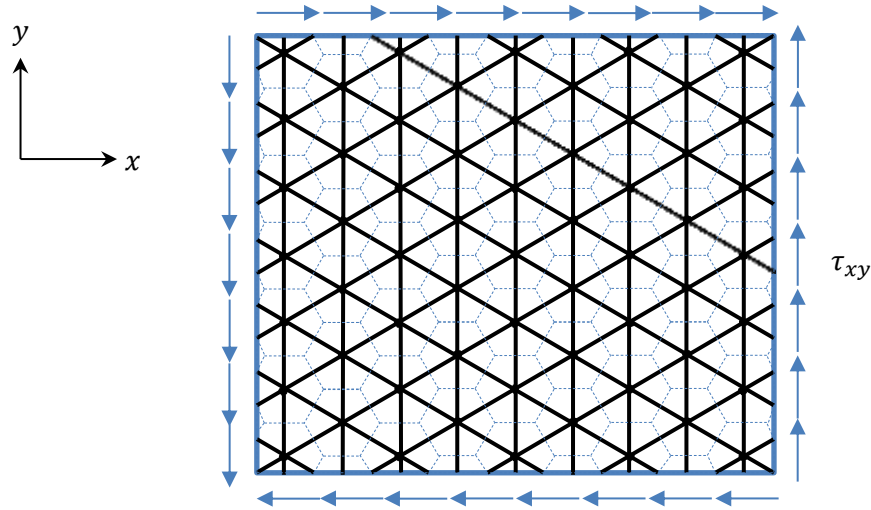


Fig. 2.8 The lattice under pure shear

For this case also the inflection points are located at the midpoint of the members, and lattice unit will be loaded as in Fig. 2.9.

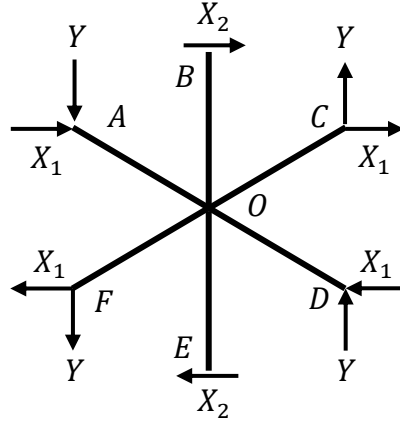


Fig. 2.9 Internal loading applied to the periodic part of the lattice under pure shear

In Fig. 2.9, the magnitude of Y is determined based on contribution of the inclined members on resisting vertical shear stresses:

$$Y = \frac{st}{2} \tau_{xy}. \quad (2.28)$$

X_1 and X_2 , in Fig. 2.9, are unknown and equilibrium along with compatibility equations must be used to obtain their values. Using the equilibrium of the moments of the forces applied to the lattice following equation is obtained:

$$X_1 + X_2 = \frac{\sqrt{3}}{2} st \tau_{xy}. \quad (2.29)$$

Since points A and C do not move relative to each other, they can be assumed to be fixed at their position by pinned supports.

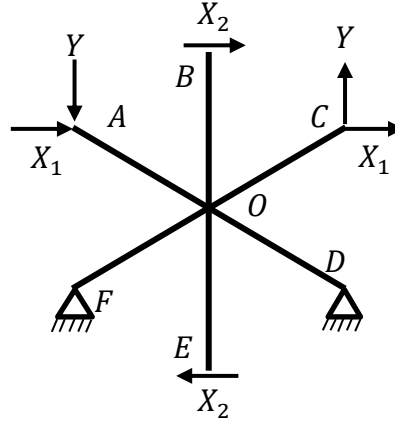


Fig. 2.10 Equivalent lattice unit of the lattice loaded in pure shear

The rotations of imaginary line AF and line BE , which indicate the shear strain, must be equal.

$$\gamma_{BE} = \gamma_{AF}. \quad (2.30)$$

To obtain γ_{EB} , relative displacement of points B and E in horizontal direction is needed:

$$\gamma_{EB} = \frac{\delta_x^{B/E}}{l_{BE}}, \quad (2.31)$$

$$\delta_{B/E} = 2 \left(\theta_o \cdot \frac{s}{2} + \frac{X_2(s/2)^3}{3EI} \right) = \theta_o s + \frac{X_2 s^3}{12EI}. \quad (2.32)$$

Anti-symmetric loaded frame, shown in Fig. 2.10, can be simplified to the frame depicted in Fig. 2.11.

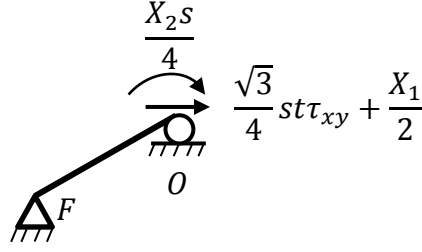


Fig. 2.11 Simplified lattice unit of the lattice loaded in pure shear

The rotation of point O is obtained as follows:

$$\theta_o = \frac{\left(\frac{\sqrt{3}}{2}X_1 + \frac{st}{4}\tau_{xy}\right) \cdot \frac{2}{\sqrt{3}s} \cdot \frac{s}{2}}{EA} + \frac{1 \cdot \frac{X_2s}{4} \cdot \frac{s}{2}}{3EI}, \quad (2.33)$$

hence, the rotation of EB is:

$$\gamma_{BE} = \frac{\delta_x^{B/E}}{l_{BE}} = \frac{6X_1 + \sqrt{3}st\tau_{xy}}{12EA} + \frac{X_2s^2}{8EI}. \quad (2.34)$$

Now, we obtain the value of γ_{AF} . For this, first the horizontal displacement of point A , in Fig. 1.10, is determined:

$$\gamma_{EB} = \frac{\delta_x^A}{l_{AF}}, \quad (2.35)$$

$$\begin{aligned} \delta_x^A = & 2 \cdot \frac{\frac{X_2s}{4} \cdot \frac{s}{8} \cdot \frac{s}{2}}{3EI} + \frac{\frac{5\sqrt{3}}{12} \cdot \left(\frac{\sqrt{3}}{2}X_1 + \frac{st\tau_{xy}}{4}\right) \cdot \frac{s}{2}}{EA} + \frac{\frac{s}{4} \cdot \left(\frac{X_1s}{4} - \frac{\sqrt{3}s^2t\tau_{xy}}{8}\right) \cdot \frac{s}{2}}{3EI} \\ & + \frac{\left(\frac{-\sqrt{3}}{2}\right) \cdot \left(-\frac{\sqrt{3}}{2}X_1 - \frac{st\tau_{xy}}{4}\right) \cdot \frac{s}{2}}{EA}. \end{aligned} \quad (2.36)$$

Simplifying the above equation, we have:

$$\delta_x^A = \frac{6X_1s + \sqrt{3}s^2t\tau_{xy}}{6EA}, \quad (2.37)$$

$$\gamma_{EB} = \frac{\delta_x^A}{l_{AF}} = \frac{6X_1 + \sqrt{3}st\tau_{xy}}{3EA}. \quad (2.38)$$

By solving equations 2.29 and 2.30 , magnitudes of X_1 and X_2 are obtained:

$$X_1 = \frac{\sqrt{3}st(s^2EA - 4EI)}{2(s^2EA + 12EI)}\tau_{xy}, \quad (2.39)$$

$$X_2 = \frac{8\sqrt{3}stEI}{s^2EA + 12EI}\tau_{xy}. \quad (2.40)$$

2.1.3.1 Shear modulus G_{xy}^{lat}

Now, shear strain is determined in terms of shear stress:

$$\gamma = \gamma_{EB} = \frac{4\sqrt{3}s^3t}{3(s^2EA + 12EI)}\tau_{xy} = \frac{1}{G_{xy}^{lat}}\tau_{xy}, \quad (2.41)$$

hence, the shear modulus is:

$$G_{xy}^{lat} = \frac{\sqrt{3}(s^2EA + 12EI)}{4s^3t}. \quad (2.42)$$

2.1.4 Isotropicity of the hexagonal lattice

Comparing the obtained Young's moduli and Poisson's ratios we see that we have necessary conditions for isotropicity of the hexagonal lattice.

$$E_x^{lat} = E_y^{lat}, \quad (2.43)$$

$$\nu_{xy}^{lat} = \nu_{yx}^{lat}, \quad (2.44)$$

If the following condition also holds, we can conclude that the lattice is isotropic.

$$G = \frac{E}{2(1 + \nu)}. \quad (2.45)$$

We can use the obtained values to check the validity of the above condition for the hexagonal lattice.

$$\frac{E^{lat}}{2(1 + \nu^{lat})} = \frac{\frac{s^2 EA + 12EI}{s^2 EA + 4EI} \cdot \frac{\sqrt{3}EA}{6st}}{2(1 + \frac{s^2 EA - 12EI}{3(s^2 EA + 4EI)})} = \frac{\sqrt{3}(s^2 EA + 12EI)}{4s^3 t}. \quad (2.46)$$

Comparing equations 2.42 and 2.46, it is concluded that the triangular lattice is isotropic.

2.1.5 Axial and flexural rigidity of the lattice members

To expect the equivalent elastic behavior from the hexagonal lattice and the material, both must have the same modulus of elasticity and Poisson's ratio. If we assume that the modulus of elasticity and Poisson's ratio of the material are E and ν respectively, then the following equations must be satisfied:

$$E^{lat} = E, \quad (2.47)$$

$$\nu^{lat} = \nu. \quad (2.48)$$

By using equations for E^{lat} and ν^{lat} , equations 2.24 and 2.27 for example, and equations 2.47 and 2.48, the axial and flexural rigidity of the members of the hexagonal lattice are determined by solving equations 2.47 and 2.48 for EA and EI :

$$EA = \frac{Est}{\sqrt{3}(1-\nu)}, \quad EI = \frac{Es^3t(1-3\nu)}{12\sqrt{3}(1-\nu^2)} \quad (2.49)$$

2.1.6 Magnitude of internal forces under σ_{xx} , σ_{yy} , and τ_{xy}

Substituting the values of axial and flexural rigidity in Eq. 2.49 into Eq. 2.8 that we obtained for magnitude of Y for the lattice under σ_{xx} , the value of this force is obtained:

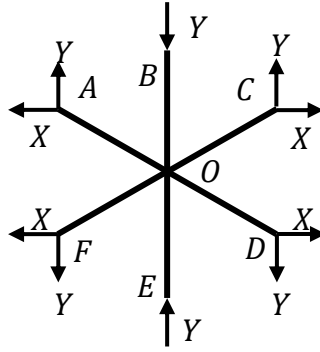


Fig. 2.12 Lattice unit under σ_{xx}

$$X = \frac{st}{2} \sigma_{xx}, \quad Y = \frac{\sqrt{3}stv}{6(\nu+2)} \sigma_{xx}. \quad (2.50)$$

If EI and EA in Eq. 2.49 are substituted in equations 2.20 and 2.21, the magnitudes of Y_1 and Y_2 applied to the lattice unit of a hexagonal lattice which is under σ_{yy} is obtained:

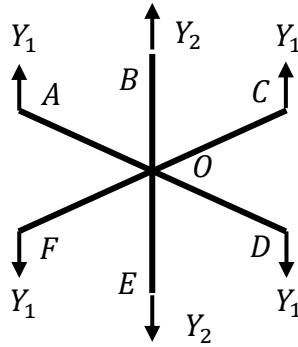


Fig. 2.13 Lattice unit under σ_{yy}

$$Y_1 = \frac{\sqrt{3}stv}{3(\nu + 2)}\sigma_{yy}, \quad Y_2 = \frac{\sqrt{3}st(3\nu + 4)}{6(\nu + 2)}\sigma_{yy}. \quad (2.51)$$

And finally, following the same procedure for lattice under pure shear, the values of X_1 and X_2 in equations 2.39 and 2.40 are determined.

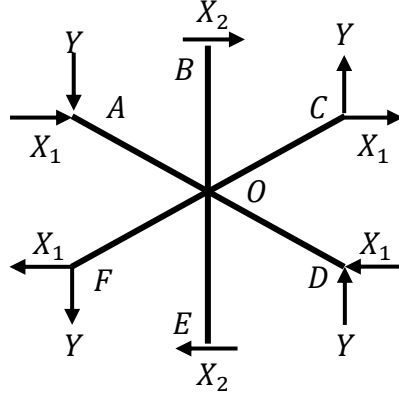


Fig. 2.14 Lattice unit under τ_{xy}

$$Y = \frac{st}{2}\tau_{xy}, \quad X_1 = \frac{\sqrt{3}st(3\nu + 2)}{6(\nu + 2)}\tau_{xy}, \quad X_2 = \frac{2\sqrt{3}st}{3(\nu + 2)}\tau_{xy}. \quad (52)$$

2.2 Critical time step

In this section, the critical time step of the explicit time integration approach used in the code is determined. The equilibrium equation for the free vibration of a single degree of freedom (SDOF) system with damping is:

$$m\ddot{x}(t) + c\dot{x}(t) + kx(t) = 0, \quad (2.53)$$

this equation used to be written in the following form:

$$\ddot{x}(t) + 2\xi\omega_n\dot{x}(t) + \omega_n^2x(t) = 0, \quad (2.54)$$

where

$$\omega_n^2 = \frac{k}{m}, \quad c = 2m\xi\omega_n, \quad (2.55)$$

here ξ is critical damping ratio and ω_n is the natural frequency. We use the Verlet method for time integration. In this method the value of acceleration at time t is obtained by using the following equation:

$$\ddot{x}(t) = -2\xi\omega_n\dot{x}(t) - \omega_n^2x(t), \quad (2.56)$$

knowing the acceleration at time t , the velocity at $t + \Delta t$ is approximated as follows:

$$\dot{x}(t + \Delta t) = \dot{x}(t) + \ddot{x}(t)\Delta t, \quad (2.57)$$

having the velocity at time $t + \Delta t$, the displacement is estimated as follows:

$$x(t + \Delta t) = x(t) + \dot{x}(t + \Delta t)\Delta t. \quad (2.58)$$

To obtain the value of the critical time step, we need to find $x(t + \Delta t)$ in terms of x at times t and $t - \Delta t$. For this, first we obtain $\dot{x}(t + \Delta t)$ in terms of $x(t)$ and $\dot{x}(t)$ by substituting Eq. 2.56 into Eq. 2.57:

$$\dot{x}(t + \Delta t) = \dot{x}(t) + (-2\xi\omega_n\dot{x}(t) - \omega_n^2x(t))\Delta t, \quad (2.59)$$

by substituting $\dot{x}(t + \Delta t)$ in the Eq. 2.59 into Eq. 2.58, we obtain:

$$x(t + \Delta t) = x(t) + (\dot{x}(t) + (-2\xi\omega_n\dot{x}(t) - \omega_n^2x(t))\Delta t)\Delta t. \quad (2.60)$$

Now, we find $\dot{x}(t)$ in terms of $x(t)$ and $x(t - \Delta t)$ by using Eq. 2.58:

$$x(t) = x(t - \Delta t) + \dot{x}(t + \Delta t)\Delta t, \quad (2.61)$$

or

$$\dot{x}(t) = \frac{x(t) - x(t - \Delta t)}{\Delta t}. \quad (2.62)$$

By substituting obtained equation for $\dot{x}(t)$ in Eq. 2.62 into E 2.60, we have:

$$x(t + \Delta t) = x(t) + \left(\frac{x(t) - x(t - \Delta t)}{\Delta t} + \left(-2\xi\omega_n \left(\frac{x(t) - x(t - \Delta t)}{\Delta t} \right) - \omega_n^2 x(t) \right) \Delta t \right) \Delta t, \quad (2.63)$$

simplifying the above equation, we obtain:

$$x(t + \Delta t) = (2 - \omega_n^2 \Delta t^2 - 2\xi\omega_n \Delta t)x(t) + (-1 + 2\xi\omega_n \Delta t)x(t - \Delta t). \quad (2.64)$$

Eq. 2.64 can be written in matrix form as follows:

$$\begin{bmatrix} x(t + \Delta t) \\ x(t) \end{bmatrix} = \begin{bmatrix} 2 - \omega_n^2 \Delta t^2 - 2\xi\omega_n \Delta t & -1 + 2\xi\omega_n \Delta t \\ 1 & 0 \end{bmatrix} \begin{bmatrix} x(t) \\ x(t - \Delta t) \end{bmatrix} = [A] \begin{bmatrix} x(t) \\ x(t - \Delta t) \end{bmatrix} \quad (2.65)$$

where matrix A is:

$$A = \begin{bmatrix} 2 - \omega_n^2 \Delta t^2 - 2\xi\omega_n \Delta t & -1 + 2\xi\omega_n \Delta t \\ 1 & 0 \end{bmatrix}. \quad (2.66)$$

Eq. 2.65 can be used to obtain the value of displacement after n and $n + 1$ time steps in terms of displacement at time zero and time Δt [Bathe 2007]:

$$\begin{aligned} \begin{bmatrix} x((n + 1)\Delta t) \\ x(n\Delta t) \end{bmatrix} &= [A] \begin{bmatrix} x((n)\Delta t) \\ x((n - 1)\Delta t) \end{bmatrix} = [A] \left([A] \begin{bmatrix} x((n - 1)\Delta t) \\ x((n - 2)\Delta t) \end{bmatrix} \right) \\ &= [A] \left([A] \left(\dots \left([A] \begin{bmatrix} x(\Delta t) \\ x(0) \end{bmatrix} \right) \dots \right) \right) = [A]^n \begin{bmatrix} x(\Delta t) \\ x(0) \end{bmatrix}. \end{aligned} \quad (2.67)$$

To have a bounded value for $x((n+1)\Delta t)$, when n goes to infinity, matrix A^n has to have bounded elements. Eigenvalues of this matrix can be used to evaluate the boundedness of its elements when it is raised to n and n tends to go to infinity. The eigenvalues of matrices A and A^n are determined by using the following equations:

$$Av = \lambda v, \quad (2.68)$$

or equivalently:

$$A^n v = \lambda^n v, \quad (2.69)$$

here v is an eigenvector of A and λ is the corresponding eigenvalue. Obviously, matrices A and A^n have the same eigenvectors, but eigenvalues of A^n are equal to the eigenvalues of A raised to n . It is clear that to have a bounded values for the elements of A^n its spectral radius($\rho(A^n)$) which is defined as below must be less than one.

$$\rho(A^n) := \max_i |\lambda_i^n|, \quad (2.70)$$

here λ_i is the i^{th} eigenvalue of matrix A . The characteristic equation of matrix A is:

$$\lambda^2 - (2 - \omega_n^2 \Delta t^2 - 2\xi \omega_n \Delta t) \lambda + 1 - 2\xi \omega_n \Delta t = 0. \quad (2.71)$$

Thus, the eigenvalues of this matrix are:

$$\lambda_{1,2} = \frac{(2 - \omega_n^2 \Delta t^2 - 2\xi \omega_n \Delta t)}{2} \pm \sqrt{\frac{(2 - \omega_n^2 \Delta t^2 - 2\xi \omega_n \Delta t)^2}{4} - (1 - 2\xi \omega_n \Delta t)}. \quad (2.72)$$

Since $\frac{(2 - \omega_n^2 \Delta t^2 - 2\xi \omega_n \Delta t)}{2}$ is a negative number, the minus sign in Eq. 2.72 needs to be selected to obtain the spectral value of matrix A .

$$\rho(A) = -\left(\frac{(2-\omega_n^2\Delta t^2-2\xi\omega_n\Delta t)}{2} - \sqrt{\frac{(2-\omega_n^2\Delta t^2-2\xi\omega_n\Delta t)^2}{4} - (1-2\xi\omega_n\Delta t)}\right). \quad (2.73)$$

To obtain the value of the critical time step, the following equation needs to be solved:

$$\rho(A) = 1. \quad (2.74)$$

Solving Eq. 2.74 for Δt_{cr} , one obtains:

$$\Delta t_{cr} = \left(\frac{2}{\omega_n}\right) \left(\sqrt{1+\xi^2} - \xi\right). \quad (2.75)$$

Hence, to have stable numerical integration, the selected time step should be less than critical one:

$$\Delta t < \left(\frac{2}{\omega_n}\right) \left(\sqrt{1+\xi^2} - \xi\right). \quad (2.76)$$

2.2.1 Critical time step of a framed structure

It has been shown that to obtain the critical time step of a framed structure one can use equation 2.75, the only difference is that instead of natural frequency, maximum frequency of the structure needs to be used in this equation:

$$\Delta t_{cr} = \left(\frac{2}{\omega_{max}}\right) \left(\sqrt{1+\xi^2} - \xi\right). \quad (2.77)$$

Maximum frequency of a framed structure can be the maximum frequency of its unsupported and undamped members, when only axial deformations are considered, because for most of structures the axial rigidity of their members is by far larger than the flexural rigidity [Cook et al. 2001]. In our case, all of the members mechanically and

geometrically are the same, therefore, only one of the members needs to be studied. Consider a uniform one-dimensional unsupported member with mass m , axial rigidity EA , and length s :

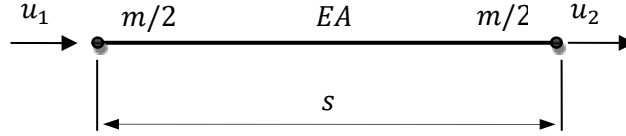


Fig. 2.15 Typical fictitious beam

where the axial rigidity is:

$$EA = \frac{Est}{\sqrt{3}(1 - \nu)}, \quad (2.78)$$

And the value of mass m in Fig. 2.15 is one third of the mass of each hexagonal particle:

$$m = \rho \left(\frac{\sqrt{3}}{6} s^2 t \right). \quad (2.79)$$

If we consider a lumped mass matrix, the equations of the free vibration of the member are:

$$\left(\frac{EA}{s} \begin{bmatrix} 1 & -1 \\ -1 & 1 \end{bmatrix} - \frac{m\omega^2}{2} \begin{bmatrix} 1 & 0 \\ 0 & 1 \end{bmatrix} \right) \begin{Bmatrix} u_1 \\ u_2 \end{Bmatrix} = \begin{Bmatrix} 0 \\ 0 \end{Bmatrix}. \quad (2.80)$$

To have nontrivial solution for the above equation, the determinant of the expression in parentheses must vanish, thus:

$$\omega^2(\omega^2 m - 4AE/s) = 0. \quad (2.81)$$

ω_{max} is obtained by solving Eq. 2.81:

$$\omega_{max} = 2\sqrt{\frac{EA}{sm}} = 2\sqrt{\frac{\frac{Est}{\sqrt{3}(1-v)}}{s\left(\frac{\sqrt{3}}{6}s^2t\right)\rho}} = 2\sqrt{\frac{2E}{\rho(1-v)s^2}} = \frac{2}{s}\sqrt{\frac{2}{(1-v)}} \cdot \sqrt{\frac{E}{\rho}} = \frac{2c}{s}\sqrt{\frac{2}{(1-v)}}, \quad (2.82)$$

Where c is the sound speed:

$$c = \sqrt{\frac{E}{\rho}}. \quad (2.83)$$

Substituting the value obtained for ω_{max} into Eq. 2.77, the critical time step for the hexagonal lattice is obtained:

$$\Delta t_{cr} = \sqrt{\frac{(1-v)}{2}} \left(\sqrt{1+\xi^2} - \xi \right) \left(\frac{s}{c} \right). \quad (2.84)$$

2.3 2D Co-rotational beam formulation

Fracturing concrete structures can experience large displacements and rotations, however, due to the quasi-brittle nature of concrete, deformations are small. In this section, co-rotational formulation is presented which permits a frame structure to have arbitrarily large displacements and rotations while the deformations are small enough to use formulations for small deformations.

2.3.1 Co-rotational concept

As a framed structure is loaded, the entire frame deforms from its original configuration. During this process the individual beam elements do the following three things, it:

- 1) rotates,
- 2) translates,
- 3) deforms.

The global displacements of the end nodes of the beam element include the information about how the beam rotated, translated, and deformed. The rotations and translations are rigid body motions that do not affect the internal forces and can be removed from the motion of the beam [Crisfield 1991]. Doing this, all that remains are the strain causing deformations of the beam element. A co-rotational formulation seeks to separate rigid body motions from strain producing deformations.

In this formulation a local coordinate system is attached to the beam element in such a way that its x-axis is always directed along this element, and rotates and translates with it. Therefore, with respect to this local co-rotating coordinate system the rigid body rotations and translations are zero and only local strain producing deformations remain.

2.3.2 Co-rotational formulation

As stated, a local coordinate system is attached to the beam element as shown in Fig. 2.16 , and rotates and translates with the beam element as the structure deforms.

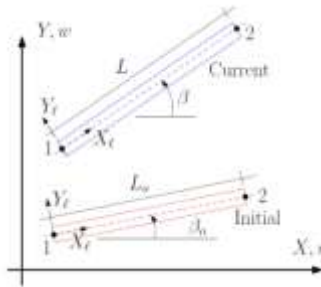


Fig. 2.16 Initial and current configuration of a typical fictitious beam

Knowing the coordinates of the two end nodes of a beam element in its initial and current configurations, initial and current angles of the co-rotating coordinate system with respect to the global coordinate system, which are denoted by β_o and β respectively, are obtained.

$$\tan \beta_o = \frac{y_2 - y_1}{x_2 - x_1}, \quad (2.85)$$

$$\tan \beta = \frac{(y_2 + w_2) - (y_1 + w_1)}{(x_2 + u_2) - (x_1 + u_1)}. \quad (2.86)$$

Here u and w are the horizontal and vertical displacements of end points respectively.

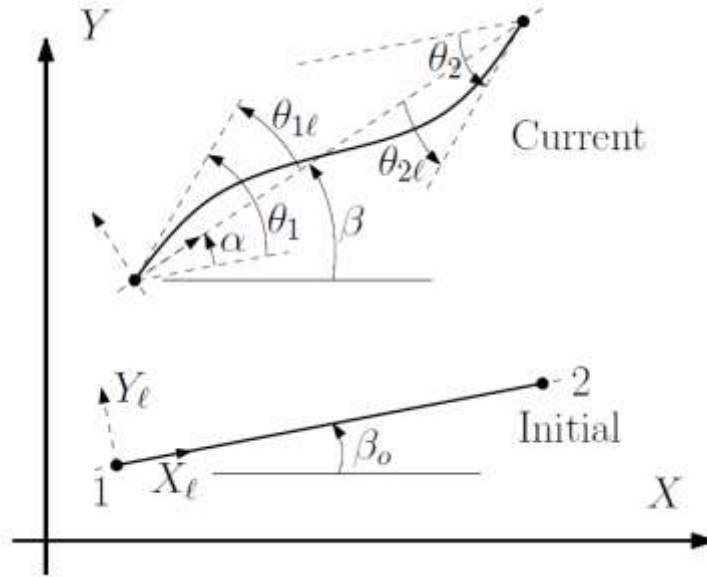


Fig. 2.17 Current deformed configuration of a fictitious beam

Angles θ_1 and θ_2 in Fig. 2.17 are the global nodal rotations calculated from rotation of hexagonal particles. Having initial and current angles of the beam and its nodal global rotations, the local nodal rotations are obtained using the following equations:

$$\theta_{1l} = \theta_1 + \beta_o - \beta, \quad \theta_{2l} = \theta_2 + \beta_o - \beta. \quad (2.87)$$

Now, it is possible to use slope-deflection formulations to obtain the moments and shear forces in nodes of the beam:

$$\begin{Bmatrix} M_{12} \\ M_{21} \end{Bmatrix} = \frac{2EI}{L} \begin{bmatrix} 2 & 1 \\ 1 & 2 \end{bmatrix} \begin{Bmatrix} \theta_{1l} \\ \theta_{2l} \end{Bmatrix}, \quad (2.88)$$

$$V_1 = \frac{M_{12} + M_{21}}{L}, \quad V_2 = -V_1, \quad (2.89)$$

where M_{ij} is the moment applied to node i of the element ij .

In this chapter the elastic lattice was formulated. The axial and flexural rigidity of its members were determined, and its isotropicity was demonstrated. An equation for critical time step of the explicit time integration, which is used in PDQ, is obtained, and the co-rotational formulation for considering large displacements was presented. In the next chapter, a damage model is defined to simulate the tensile fracture of concrete.

Chapter 3 Damage model

In this chapter we will propose a new formulation to simulate the fracture of concrete under tension, and in the next chapter we will show that the new formulation is capable of appropriately simulating the tensile fracture of the concrete.

3.1 Micropolar damage model

In our proposed damage model, constitutive material model, the softening characteristic of quasi-brittle material such as concrete is simulated by correcting the initial linear elastic forces using a damage parameter. A modifier coefficient, which is in terms of a parameter that is called the damage index and denoted by ω , is applied to the elastic force. As long as the material is in the elastic range, this parameter is assumed to be zero. Based on our formulation, the axial force in the lattice members are obtained using the following equations:

$$N(i) = (1 - \omega)EA\epsilon_a + N_{dampij}, \quad (3.1)$$

$$N(j) = -N(i), \quad (3.2)$$

where ω is the damage index and ϵ_a is the axial stretch of the fictitious beam defined as follows:

$$\epsilon_a := \frac{\Delta d}{s}. \quad (3.3)$$

Here Δd is the axial deformation of the fictitious beam and s is its initial length. N_{dampij} is the damping force that has been defined to damp the waves produced in the solution process. To obtain its value, the relative translational velocity vector, v_{ij} , between particles i and j is computed. Then the damping force, N_{dampij} , between the two particles is given by:

$$N_{dampij} = -\zeta |N_{elastij}| \frac{v_{ij}}{|v_{ij}|}, \quad (3.4)$$

where ζ is the damping factor, with value set assumed to be 0.05, and $N_{elastij}$ is the elastic inter-particle force calculated in the previous section, including the effect of damage. Thus, the damping force, being some proportion of the elastic force magnitude, and always opposing the direction of motion [Gerstle et al. 2014]. The end moments applied to the fictitious beams are obtained using the following equations:

$$M_{ij} = (1 - \omega) \frac{2EI}{s} (2\theta_{il} + \theta_{jl}), \quad (3.5)$$

$$M_{ji} = (1 - \omega) \frac{2EI}{s} (2\theta_{jl} + \theta_{il}), \quad (3.6)$$

where θ_{il} and θ_{jl} are local rotations in the co-rotational formulations. Using the equilibrium of the fictitious beam the values of nodal shear forces are determined:

$$V(i) = \frac{M_{ij} + M_{ji}}{s}, \quad (3.7)$$

$$V(j) = -V(i). \quad (3.8)$$

3.2 Tensile damage index

To include the effect of axial and flexural deformations of the fictitious beam on its damage, we define a new stretch which is combinations of these two:

$$\epsilon_{mp} = \epsilon_a + \beta s \psi_z. \quad (3.9)$$

We call the new stretch micropolar stretch. Here β is a dimensionless parameter which is chosen to be 0.1 to replicate the ratio of uniaxial compressive load to uniaxial tensile load, usually around ten, as is observed empirically for normal-strength concrete. The effect of other values for this parameter, which indicates the contribution of curvature in the fictitious beam's damage, can be investigated. ψ_z is the maximum of the absolute value of the fictitious beam's curvature. Since

there is no transverse loading applied to the fictitious beam, curvature is maximum at one of its ends and therefore is determined using the following equation:

$$\psi_z := \max \left(\left| \frac{2}{S} (2\theta_{il} + \theta_{jl}) \right|, \left| \frac{2}{S} (2\theta_{jl} + \theta_{il}) \right| \right). \quad (3.10)$$

To define the damage index, we first need to define the relationship between force and micropolar stretch. Inspired by bilinear damage model, used in finite element methods to simulate the tensile fracture of concrete, we assume that the force-micropolar stretch relationship is bilinear as shown in Fig. 3.1.

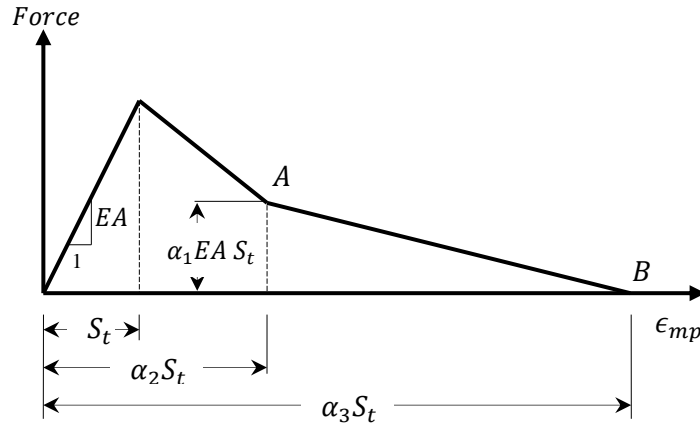


Fig. 3.1 Bilinear softening model used to define the damage index

Based on this model, as long as the value of micropolar stretch is less than S_t , which is a parameter that needs to be calibrated using experimental results, the fictitious beam is elastic and damage index is assumed to be zero. When the value of the micropolar stretch becomes greater than S_t , but it is still less than $\alpha_3 S_t$, the fictitious beam experiences softening and so damage; α_1 , α_2 , and α_3 are the other parameters which have been used to define the damage index.

When the micropolar stretch is greater S_t and is less than $\alpha_2 S_t$ internal force in the fictitious beam can be obtained by using the graph in Fig. 3.1:

$$F = EAS_t - (\epsilon_{mp} - S_t) \left(\frac{EAS_t - \alpha_1 EAS_t}{\alpha_2 S_t - S_t} \right) = EA \left(\frac{(\alpha_2 - \alpha_1)S_t - (1 - \alpha_1)\epsilon_{mp}}{\alpha_2 - 1} \right) \quad (3.11)$$

Now we are ready to define the damage parameter. For this, we assume that the axial force can also be obtained using the following equation:

$$F = (1 - \omega)EA\epsilon_{mp} . \quad (3.12)$$

Note that this is only an assumption and the axial load is determined by equation (3.1), and Eq. 3.12 is defined to obtain an expression for the damage index. Damage index is determined by solving equations 3.11 and 3.12 for ω :

$$\omega = \left(\frac{\alpha_2 - \alpha_1}{\alpha_2 - 1} \right) \frac{\epsilon_{mp} - S_t}{\epsilon_{mp}} . \quad (3.13)$$

When the value micropolar stretch is greater than $\alpha_2 S_t$ and is less than $\alpha_3 S_t$, we use the same procedure to obtain the damage index, the results is:

$$\omega = 1 - \left(\frac{\alpha_1}{\alpha_3 - \alpha_2} \right) \frac{\alpha_3 S_t - \epsilon_{mp}}{\epsilon_{mp}} . \quad (3.14)$$

If the value of the micropolar stretch is greater than $\alpha_3 S_t$, we will assume that the fictitious beam is completely damaged and is no longer functional. This is equivalent to assuming one for the value of damage parameter. An important assumption is that the damage parameter here decreases with time, therefore, the damage index is determined from the following equations:

$$\omega = \begin{cases} \max(0, \omega_{prev}) & \epsilon_{mp} \leq S_t \\ \max\left(\left(\frac{\alpha_2 - \alpha_1}{\alpha_2 - 1}\right) \frac{\epsilon_{mp} - S_t}{\epsilon_{mp}}, \omega_{prev}\right) & S_t < \epsilon_{mp} \leq \alpha_2 S_t \\ \max\left(1 - \left(\frac{\alpha_1}{\alpha_3 - \alpha_2}\right) \frac{\alpha_3 S_t - \epsilon_{mp}}{\epsilon_{mp}}, \omega_{prev}\right) & \alpha_2 S_t < \epsilon_{mp} \leq \alpha_3 S_t \\ 1 & \epsilon_{mp} > \alpha_3 S_t \end{cases} , \quad (3.15)$$

where ϵ_{mp} is the current micropolar stretch and ω_{prev} is the value of the damage index in the previous time step. In summary, based on the value of the micropolar stretch and the damage index in the previous time step, the damage index in current time step is determined by using the equations in 3.15.

Before we proceed to calibrate the model, discussion regarding mesh dependency is needed. The micropolar stretch in Eq. 3.9 is a function of the length of the fictitious beams, so that damage index in Eq. 3.15 is also a function of the length of the fictitious elements. As a result, the parameters of the damage index are a function of the length of the fictitious beams and for each size of these elements a new calibration is needed.

In the next chapter experimental results of notched three-point-bending beams will be used to calibrate proposed damage models and determine proper values for the unknown parameters in the equations above.

Chapter 4 Calibration of the damage model

In this chapter the diagrams of crack mouth opening displacement (CMOD) vs. load of notched three-point-bending beams are used to calibrate the damage model proposed in the chapter three. These data are provided by the experiments which have been done based on a proposed test method of ACI 446-5 by Chapman [Chapman 2011]. Twelve specimens were cast in three different sizes that will be introduced in the next section.

4.1 Configuration of the beams and material properties of the concrete

The configuration of the specimens is given in Fig. 4.1. As stated the beams have been casted in three different nominal sizes that are given in Table 1. We call these beams D3, D6, and D9; denoting beams with 3 , 6, and 9 inches of depth respectively. It is worth noting that the reason for overhangs is to prevent sudden failure of the specimens before end of the tests by producing negative moment at mid-span.

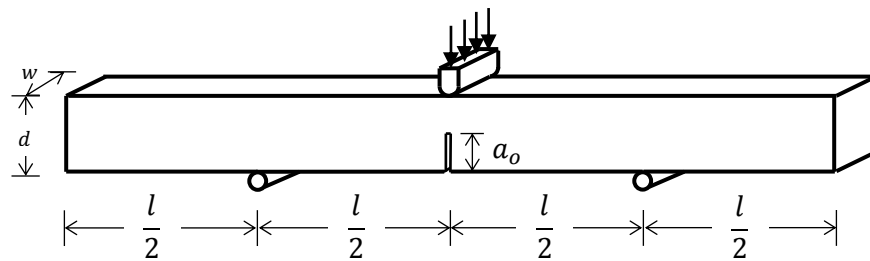


Fig. 4.1 Configuration of the beam specimens

Table 4.1 Nominal beam dimensions in mm

Beam Group	Depth (d)	Width (w)	Span (l)	Notch Depth (a _o)	Notch Width
D3	76.2	152.4	228.6	25.4	2.54
D6	152.4	152.4	457.2	50.8	2.54
D9	228.6	152.4	685.8	76.2	2.54

The material properties of the concrete that we need for our models are density, Poisson's ratio and modulus of elasticity. These values for the concrete used in experiments are 2323 (kg/m³), and 30 (GPa), and 0.2 respectively.

4.2 Simplification in configuration of beams

The configuration of beams in computational models are slightly different from that in experiments. To decrease the computational cost, overhangs are eliminated in the computational models and instead two negative moments, as shown in Fig. 4.2, are applied to the both ends of the beams.

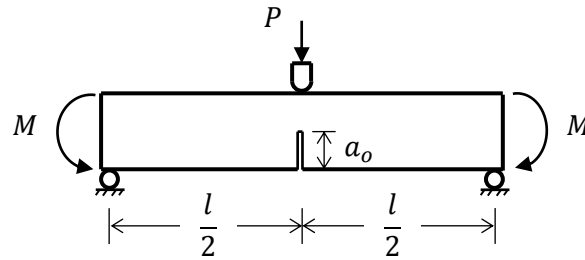


Fig. 4.2 Overhangs are replaced with equivalent moment

Since the self-weight of the beams are not included in our models, the magnitude of the negative moments is equal to the magnitude of the moment in the center of the beams in the experiments under the beams self-weight. These values for beams D3, D6, and D9, in N.mm, are 1,840, 9,120, and 22,330 respectively. The influence of these moments on the force-CMOD diagrams of the beams is negligible, because of their small magnitude, but in order to simulate the experimental situations exactly these moments are included in the models.

4.3 Loading specifications

In this section the way the loads are applied in computational models is introduced. For this, the geometry of D3 beam modeled by using PDQ is provided in Fig. 4.3. The loading has two stages: first the negative moments are applied to the end of the beams, and after applying these moments the vertical load is applied in the center top of the computational beams. To apply the vertical load, we have included an extra particle in the center top of the beam, the particle is in dark blue in Fig. 4.3.

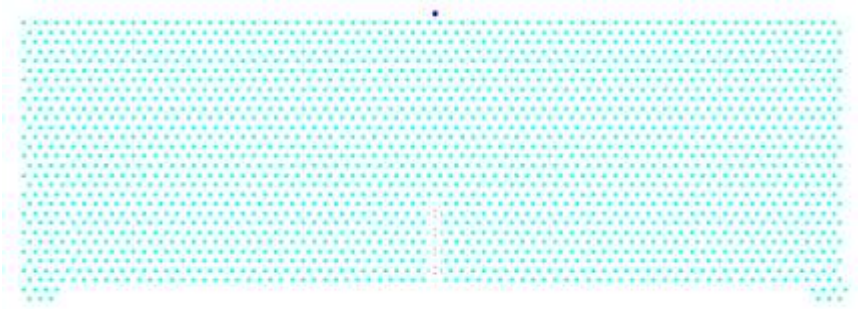


Fig 4.3 Computational model of D3 beam, lattice spacing, s , is 3.175 mm

To apply the vertical load the deformation control method is used, which means that a fixed amount of downward displacement is applied to the center top particle in each time step and the deformation is slowly increased. Since this particle is interacting with the surrounding particles, the vertical component of the applied forces exerted to the particle is computed. The magnitude of this force together with crack mouth opening displacement (CMOD), these data, are recorded as the vertical displacement of this particle increases. I need to add that to simulate the notch in the models the particles that are in the region where the notch is located are eliminated, and also the damage index, ω ,

of the fictitious beams which are located on this region and their spacing is equal to the lattice spacing is assumed to be one, so they are not allowed to interact.

Before proceeding to calibrate the proposed damage model, the maximum value of the velocity that can be applied to the top particle in order to prevent waves and dynamic effects in the models is obtained, and also the highest value of the time step which guarantees accuracy of time integration is determined. Furthermore, the effect of unknown parameters of the damage model on the CMOD-load diagram is investigated.

4.4 Maximum value of velocity applied to the top particle

Different values of velocity were applied to the top particle and CMOD-load diagrams of the models were plotted and its effect on these diagrams is monitored; the velocity is obtained by dividing the value of displacement applied to the top center particle in each time step by the value of the time step. The upshot is that when the velocity is less than 0.08 m/s some vibration in the center top particle is observed, since the top center particle is monitored, but the overall shape of the diagram do not change. Because the dynamic effect of loading is negligible for this value of speed, it is used for calibrating the models and finally a lower value is used to smoothen the graphs.

4.5 Maximum value of the critical time step

In explicit time integration methods, the value of the time step needs to be smaller than the critical one in order to guarantee the stability of the solution. In addition, this value needs to be restricted to a value which guarantees the accuracy of solution as well. We have checked different values of time step to obtain the maximum value of time step

which gives satisfactory accurate solutions. As a result, when the time step is chosen as twenty five percent of the critical time step, the solution is sufficiently accurate:

$$\Delta t = \frac{1}{4} \sqrt{\frac{(1-\nu)}{2}} \left(\sqrt{1+\xi^2} - \xi \right) \left(\frac{S}{c} \right). \quad (4.1)$$

4.6 Effect of parameters of damage model on the CMOD-load diagram

The damage model has four parameters which need to be calibrated. Determining these values using trial and error without having any clue that how crack mouth opening displacement-load diagram is affected by these parameters is very difficult. Therefore, first the effect of each parameter on the shape of the typical load-CMOD diagram, shown in Fig. 4.4, were investigated and the following conclusions were drawn:

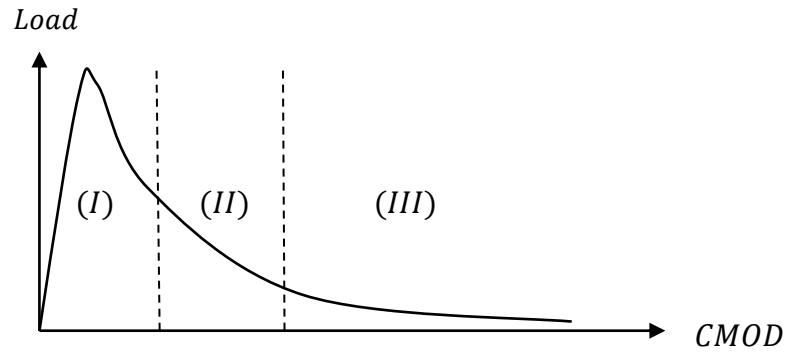


Fig. 4.4 Typical CMOD-load diagram

- α_1 and α_3 have almost the same effect on the shape of the diagram and both affect the shape of diagram in regions (II) and (III) . However, α_3 has more influence on the shape of the tail of the diagram, region (III). Thus, α_1 is changed to control

the shape of the diagram in the region (II) and shape of the diagram in region (III) is controlled by α_3 .

- α_2 mostly affect region (I) of the diagram and the peak load. Therefore, this parameter is used to control the peak load.
- S_t affects all of the three regions of the diagram.

Keeping the above hints in mind, three different lattice spacing have been chosen and the damage model has been successfully calibrated. As stated in chapter three, the damage model is influenced by the lattice particle spacing, s , used in modeling. Therefore, the model is calibrated for three different size of lattice spacing: 3.175, 6.35, and 12.7 mm. The obtained results for three different beam sizes (D3, D6, D9) and for the three different size of lattice spacing are represented below.

4.7 Calibration of the damage model for $s = 3.175$ mm

The model was calibrated for the smallest lattice spacing and the following values for the parameters, for the best correspondence with experimental results, were obtained:

Table 4.2 The value of damage model parameters for $s = 3.175$ mm

S_t	α_1	α_2	α_3
0.00015	0.13	20.0	415

CMOD-load diagrams for numerical simulations and experiments are given in figures 4.5, 4.6, and 4.7 respectively. The experimental results fall in the area which shaded in light gray in these figures. Comparing numerical and experimental results, it can be seen that the proposed model is capable of successfully simulating the fracture of plain concrete beam in tension.

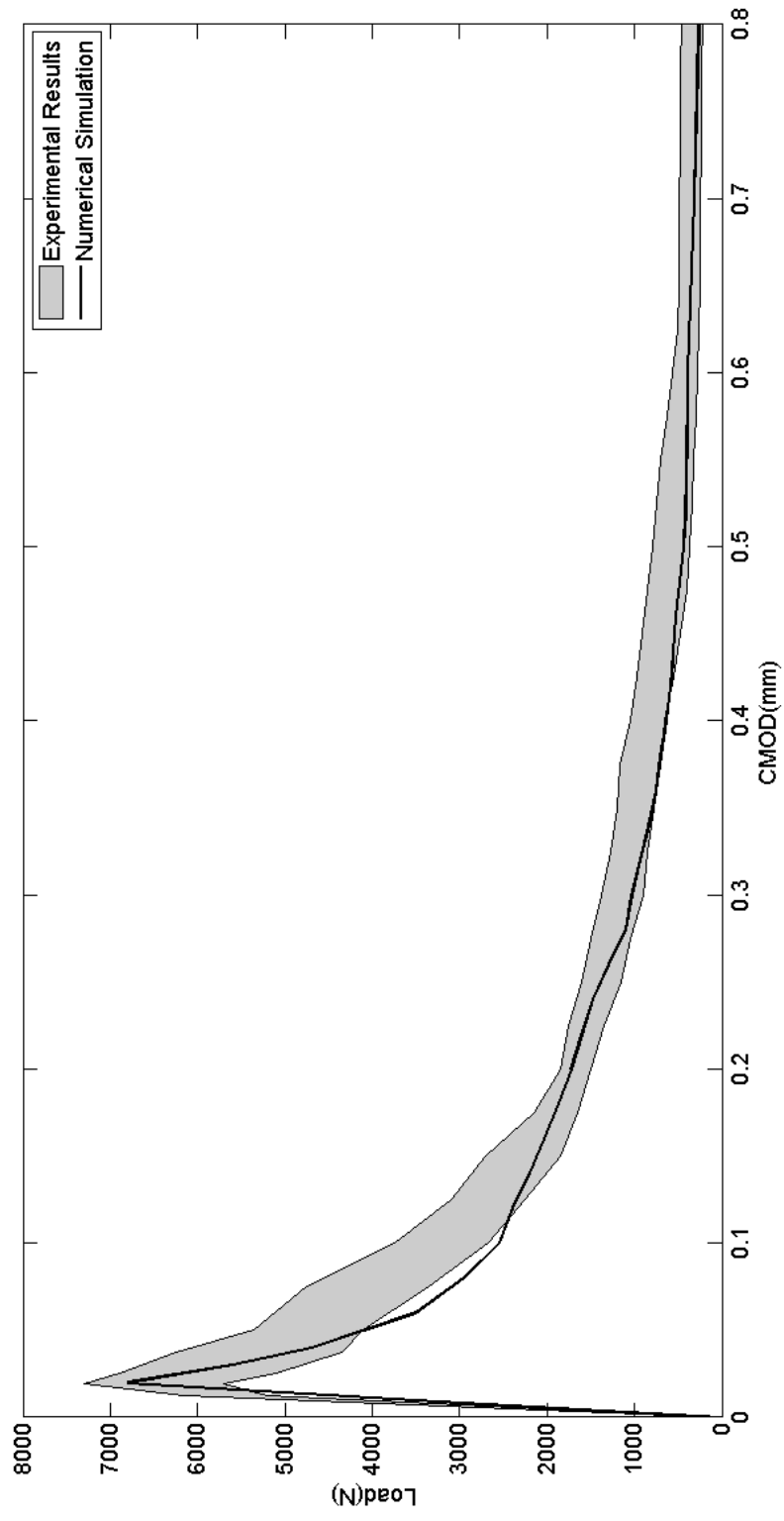


Fig. 4.5 Numerical and experimental results for CMOD- load of D3 beam, $s = 3.175$ mm

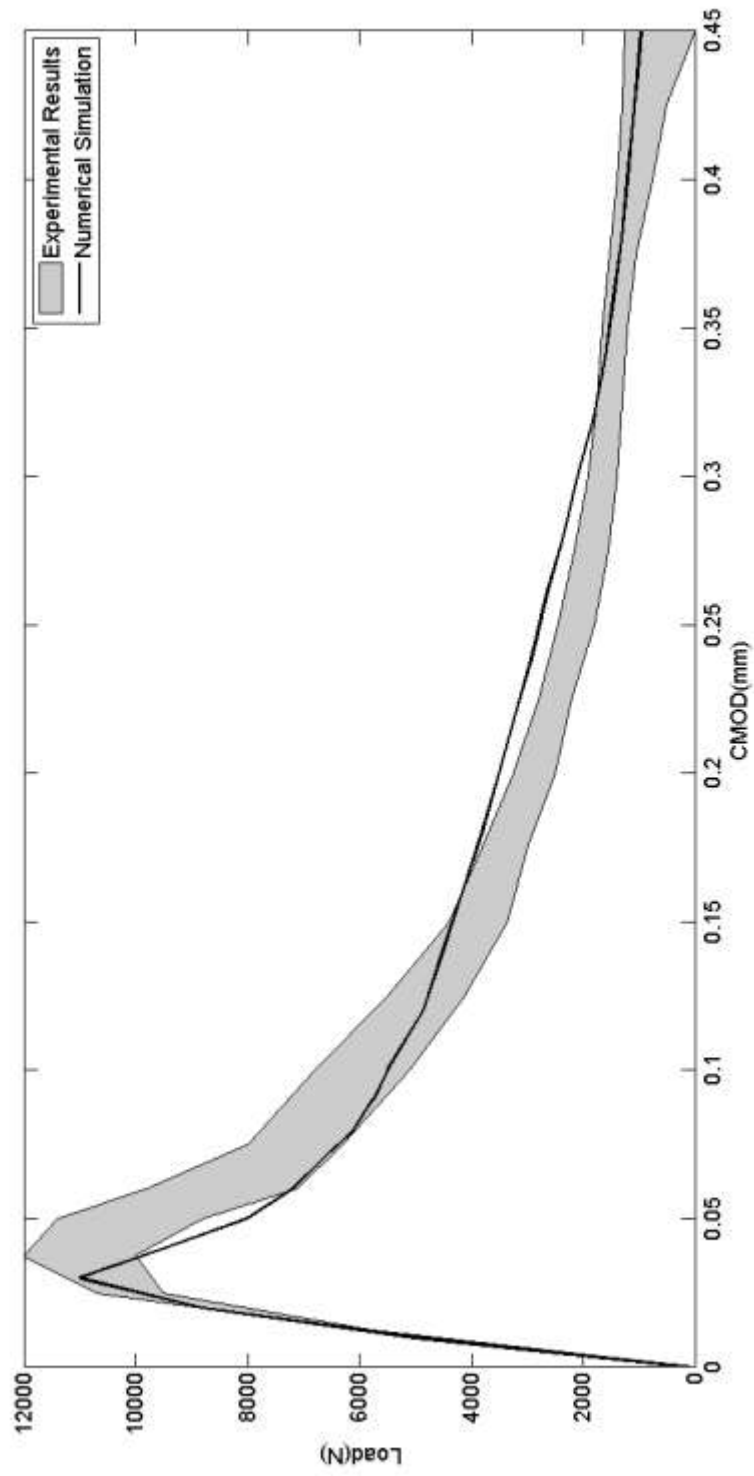


Fig. 4.6 Numerical and experimental results for CMOD-load of D6 beam, $s = 3.175$ mm

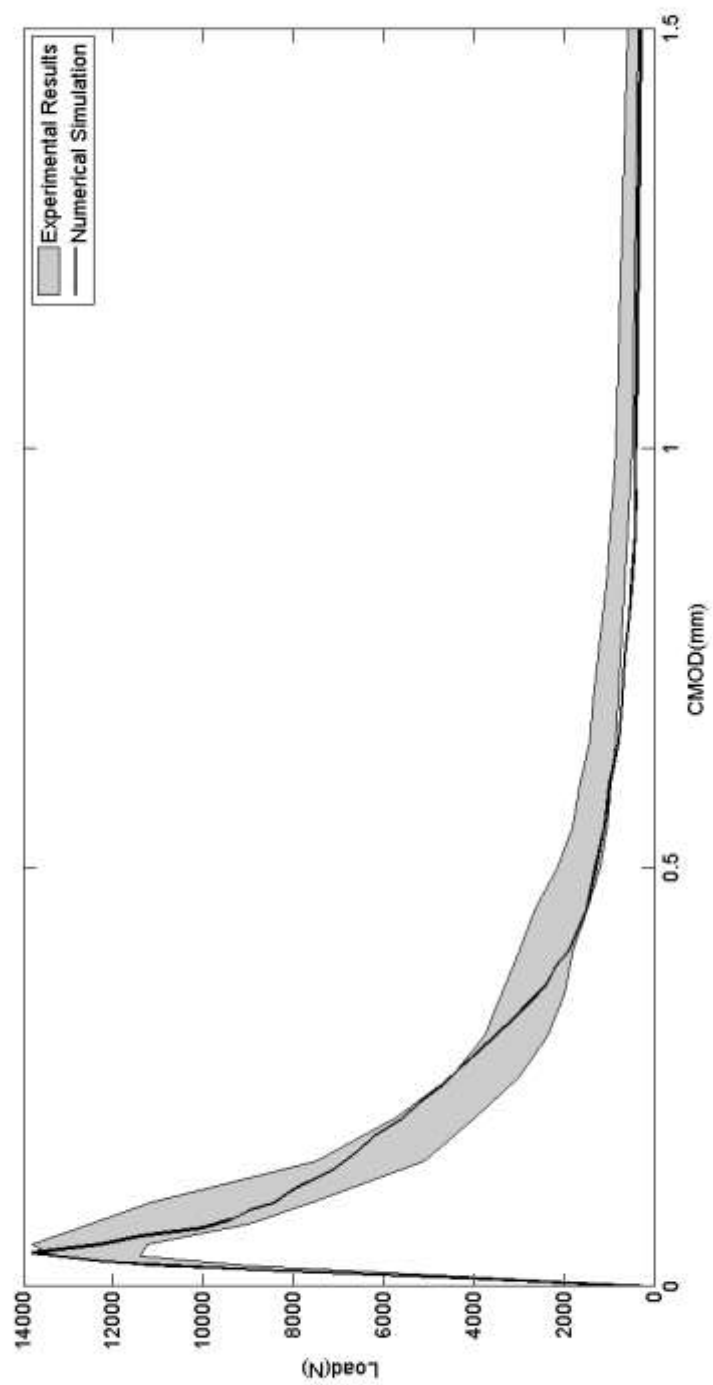


Fig. 4.7 Numerical and experimental results for CMOD-load of D9 beam, $s = 3.175$ mm

As Chapman has stated in his thesis [Chapman, 2011] two different approaches have been used to do the experiments. The experiments have been done on D6 beam first, and the loading rate has been too fast, so that sudden dynamic failure has been occurred during the loading. Consequently, different experimental approach has been used to exclude dynamical effects for D3 and D9 beams. If one compares the value of CMOD of D3 and D6 beams, when the specimens fail, in figures 4.5 and 4.6, he/she can see that this value is smaller for the bigger beam, which can indicate the faster loading rate of D6 beam. Surprisingly, the correspondance of the numerical and experimental results is better for D3 and D9 beams and the damage model is capable of distinguishing between two different experimental approaches.

4.7.1 Numerical and experimental results for load point displacement

Crack mouth opening displacement is not sensitive to concrete damage in loaded points and also deformation of supports. On the other hand, the the load point displacement (LPD) is very sensitive to the damage of concrete in loaded points and since the beams maximum displacement is about 1 mm, see figures 4.8, 4.9, and 4.10, the results obtained for the displacement of the midpoint are not generally reliable and are not used by researchers as dependable results. In the figures 4.8, 4.9, and 4.10 the numerical and experimental diagrams for LPD- load is given. As it can be seen, there is a good agreement between experimental and numerical results which indicates reliability of experimental results and accuracy of the formulation and dependability of the damage model. However, there is a considerable difference between the results in elastic range for D6 beam. Owing to the fact that the results obtained for the elastic response of D3 and D9 beams are in good agreement with experimental results and the same procedure

is used to computationally simulate the three beams, the reason for this difference is not clear and can be the different approach used to do the experiments on D6 beam.

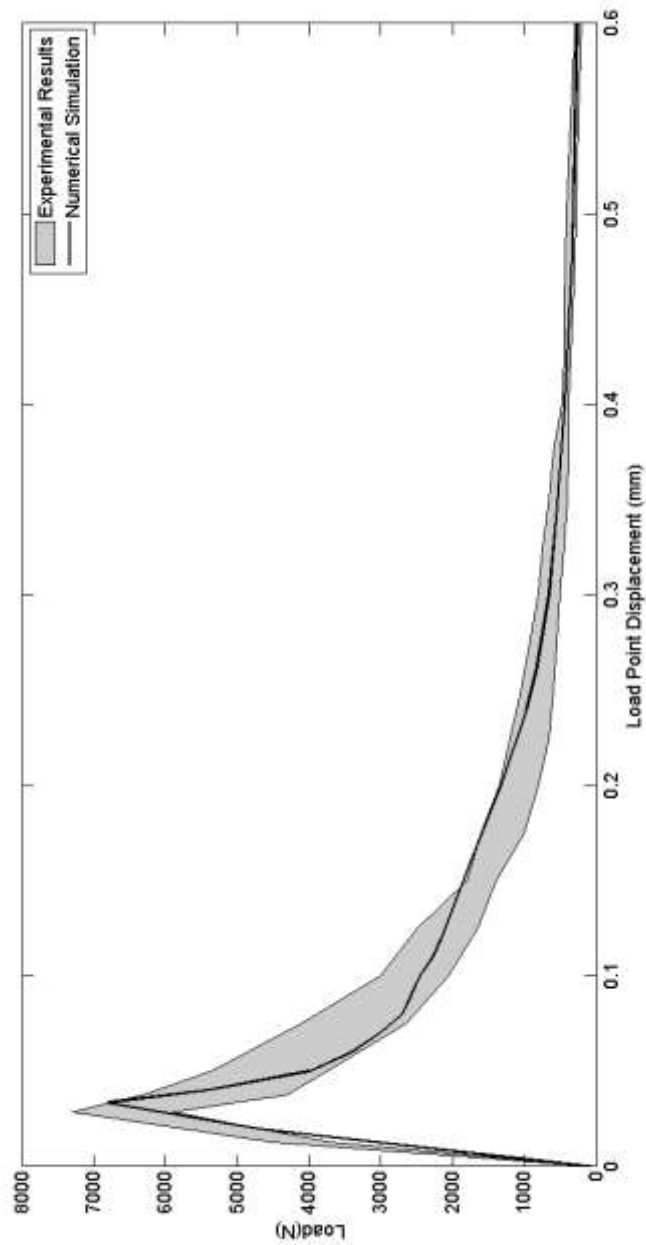


Fig. 4.8 Numerical and experimental results for LPD-load of D3 beam, $s = 3.175$ mm

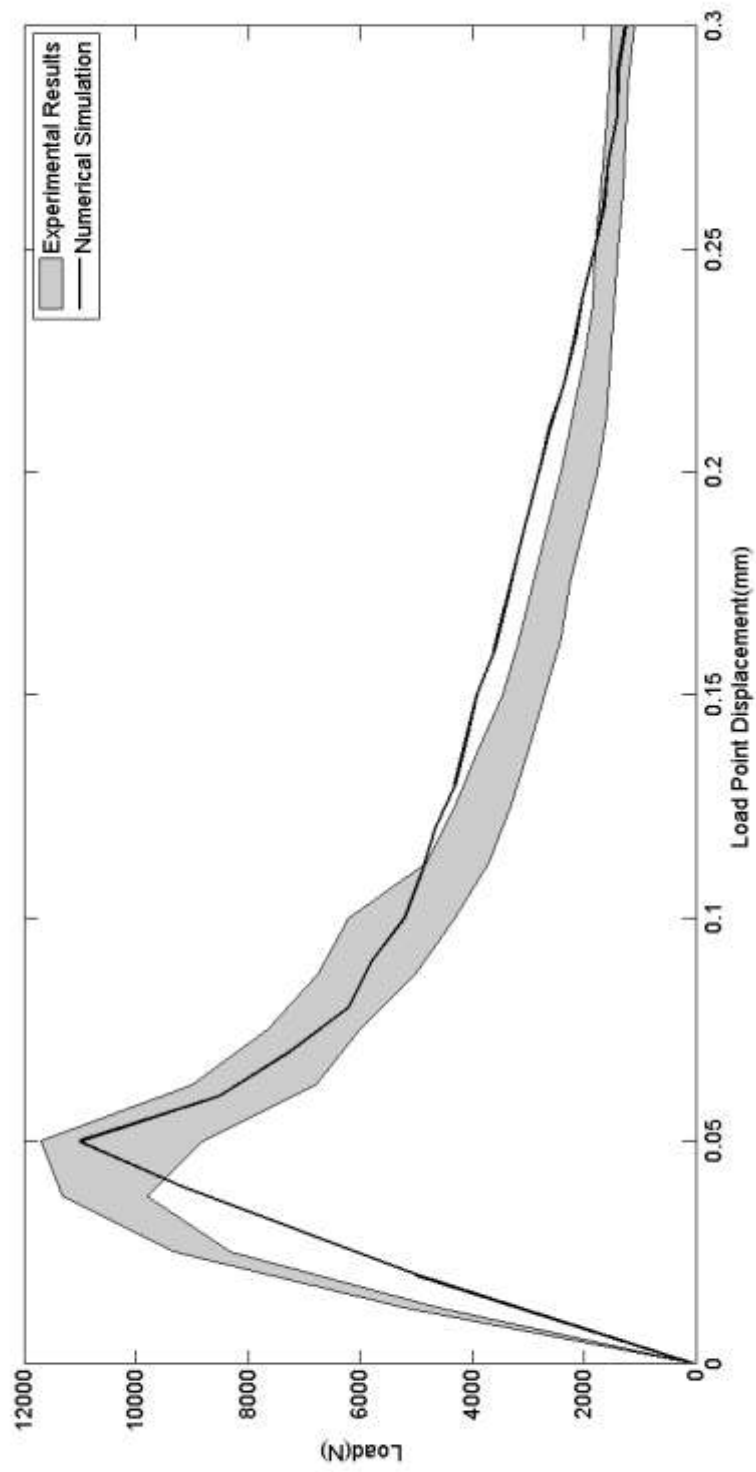


Fig. 4.9 Numerical and experimental results for LPD-load of D6 beam, $s = 3.175$ mm

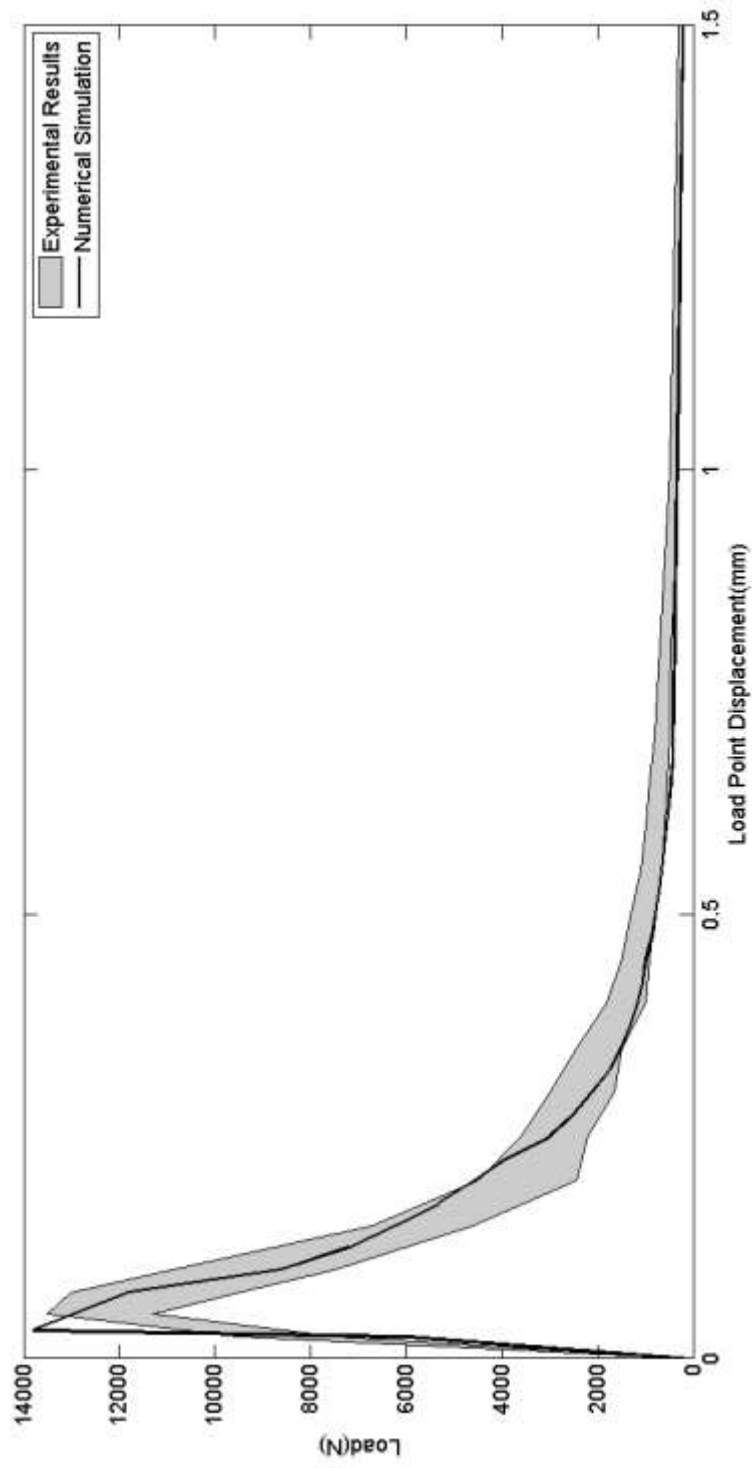


Fig. 4.10 Numerical and experimental results for LPD-load of D9 beam, $s = 3.175$ mm

4.7. 2 Damage and cracking pattern

The main goal of this research is to calibrate the damage model using the experimental CMOD-load diagrams. Since the length and width of the cracking process zone and the length of the cracks are not measured during conducting laboratory experiments, no conclusion can be made from the results obtained from simulations. However, to show the pattern of FPZ and cracking predicted by the simulations the results are presented for only one beam for each size of lattice spacing.

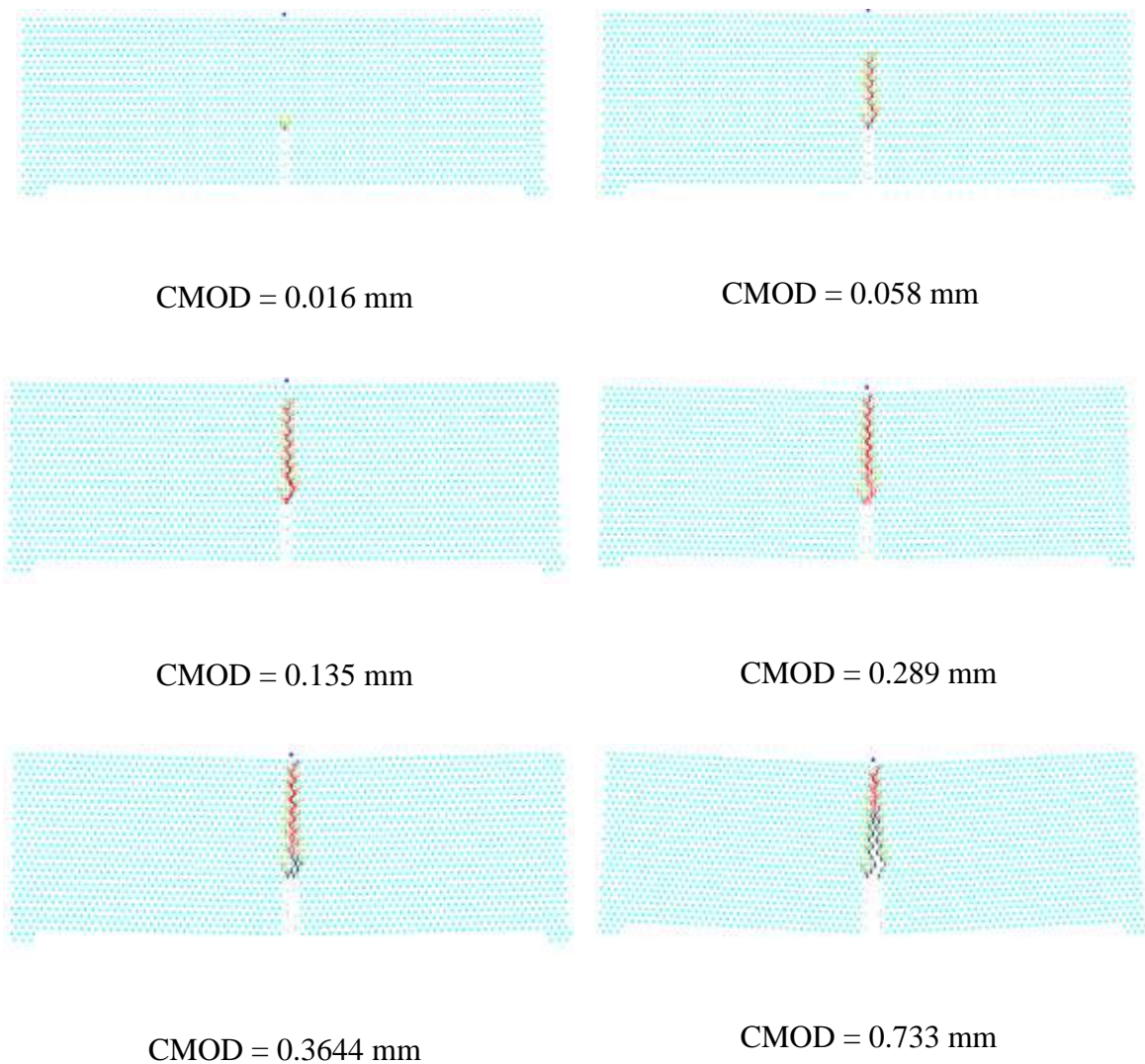
Fig. 4.11 shows damage and cracking propagation for six different values of CMOD. We have used four different colors to distinguish the damaged links. The damage range for different colors is different, which is given in table 4.3.

Table 4.3 The color of the damaged fictitious beam based on the range of damage

Color:	yellow	orange	brown	red
Damage index range:	0.0 to 0.3	0.3 to 0.6	0.6 to 0.8	0.8 to 1.0

When the damage index of a link reaches one, we eliminate that link which means that we let the crack to propagate and show the surfaces of the new crack with a black line.

As can be seen, the length of the FPZ is big and reaches the top of the beam before cracking happens, and racking initializes after the beam lose most of its strength, due to formation and grow of the micro-cracks in FPZ. The crack direction is vertical which is in correspondence with experimental observations.



Color:	yellow	orange	brown	red
Damage index range:	0.0 to 0.3	0.3 to 0.6	0.6 to 0.8	0.8 to 1.0

Fig. 4.11 Damage pattern of D3 beam for different values of CMOD, see Fig. 4.5 for corresponding load values, $s = 3.175$ mm

4.8 Calibration of the damage model for $s = 6.35$ mm

In this section, we calibrate the damage model for the lattice spacing 6.35 mm. To decrease the complexity of the damage model, we attempted to use the same values of α_1 , α_2 , and α_3 that we obtained for $s = 3.175$ mm and recalibrate the model only by determining a new value for S_t . Fortunately, the damage model could be recalibrated by assuming 0.000118 for the value of S_t . The parameters of the damage model for the new lattice spacing are given in table 4.4.

Table 4.4 The value of damage model parameters for $s = 6.35$ mm

S_t	α_1	α_2	α_3
0.000118	0.13	20.0	415

Figures 4.12, 4.13, and 4.14 represent the obtained CMOD-load diagrams for three different beam sizes and comparison of them with the experimental results. Interestingly, the numerical results are in good agreement with the experimental for D3 and D9 beams and to somehow deviate from that for D6 beam. Since the LPD-load diagrams do not provide new information, they are not included for this lattice spacing here.

Damage and cracking pattern for six different values of CMOD of D6 beam are given in Fig. 4.15. The same conclusions can be made by comparing the values of CMOD and the damage and cracking patterns.

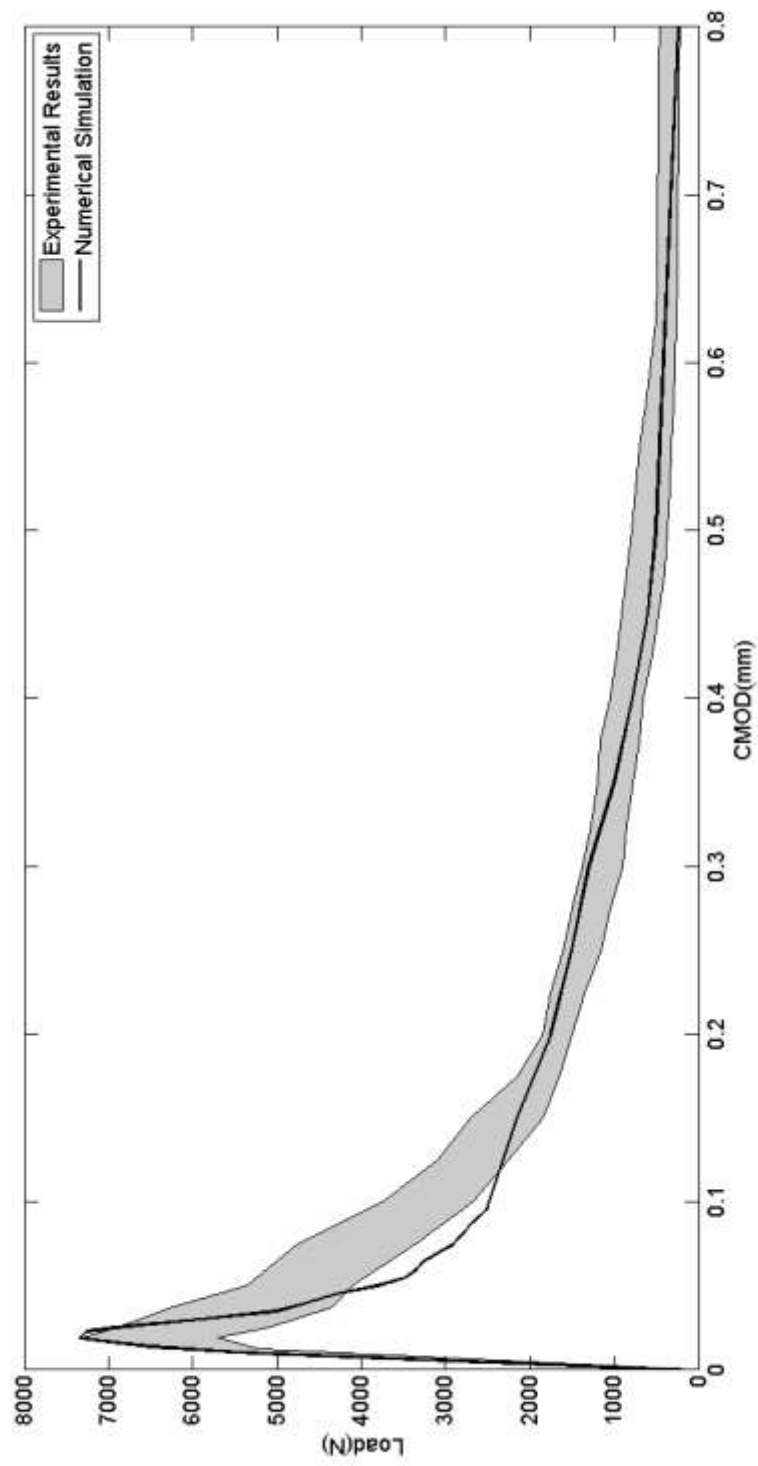


Fig. 4.12 Numerical and experimental results for CMOD-load of D3 beam, $s = 6.7$ mm

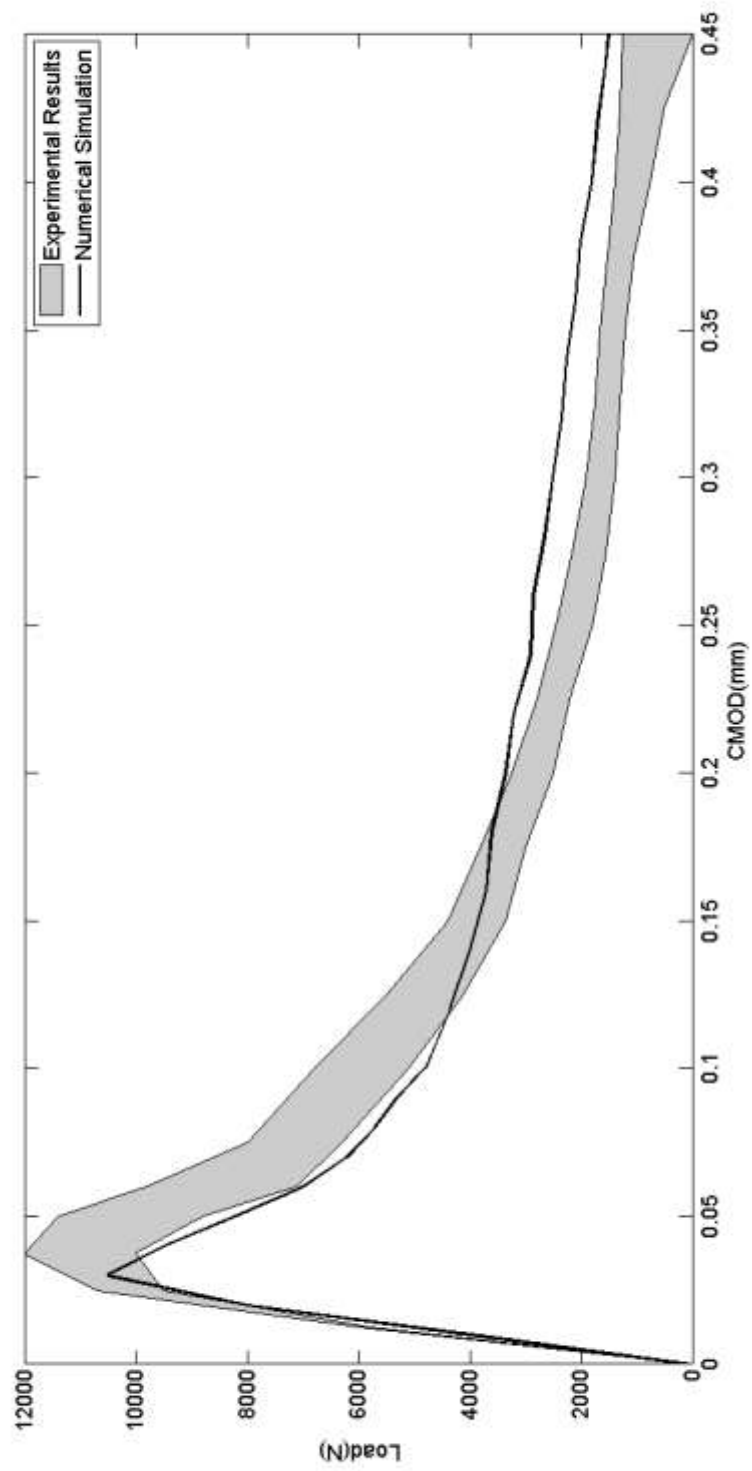


Fig. 4.13 Numerical and experimental results for CMOD-load of D6 beam, $s = 6.35$ mm

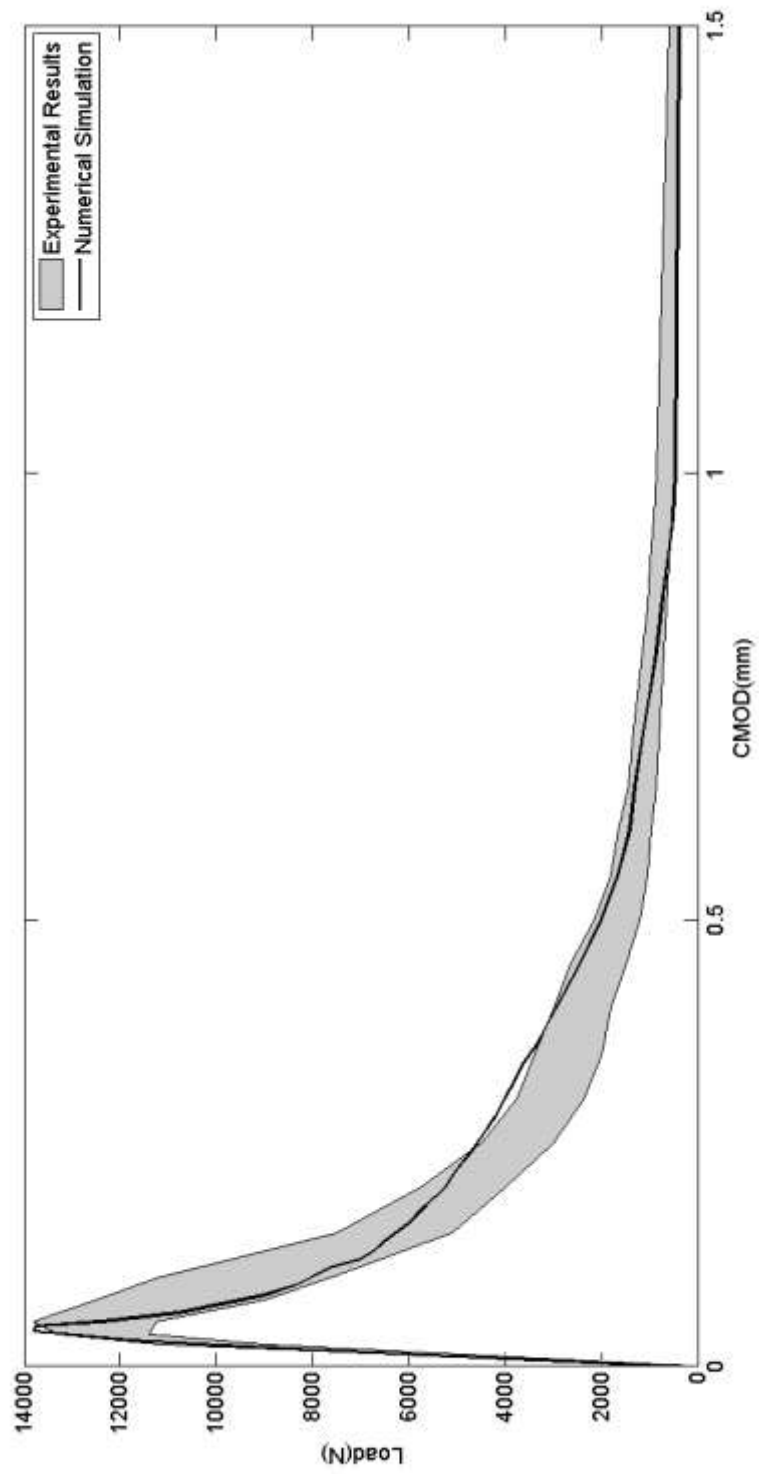
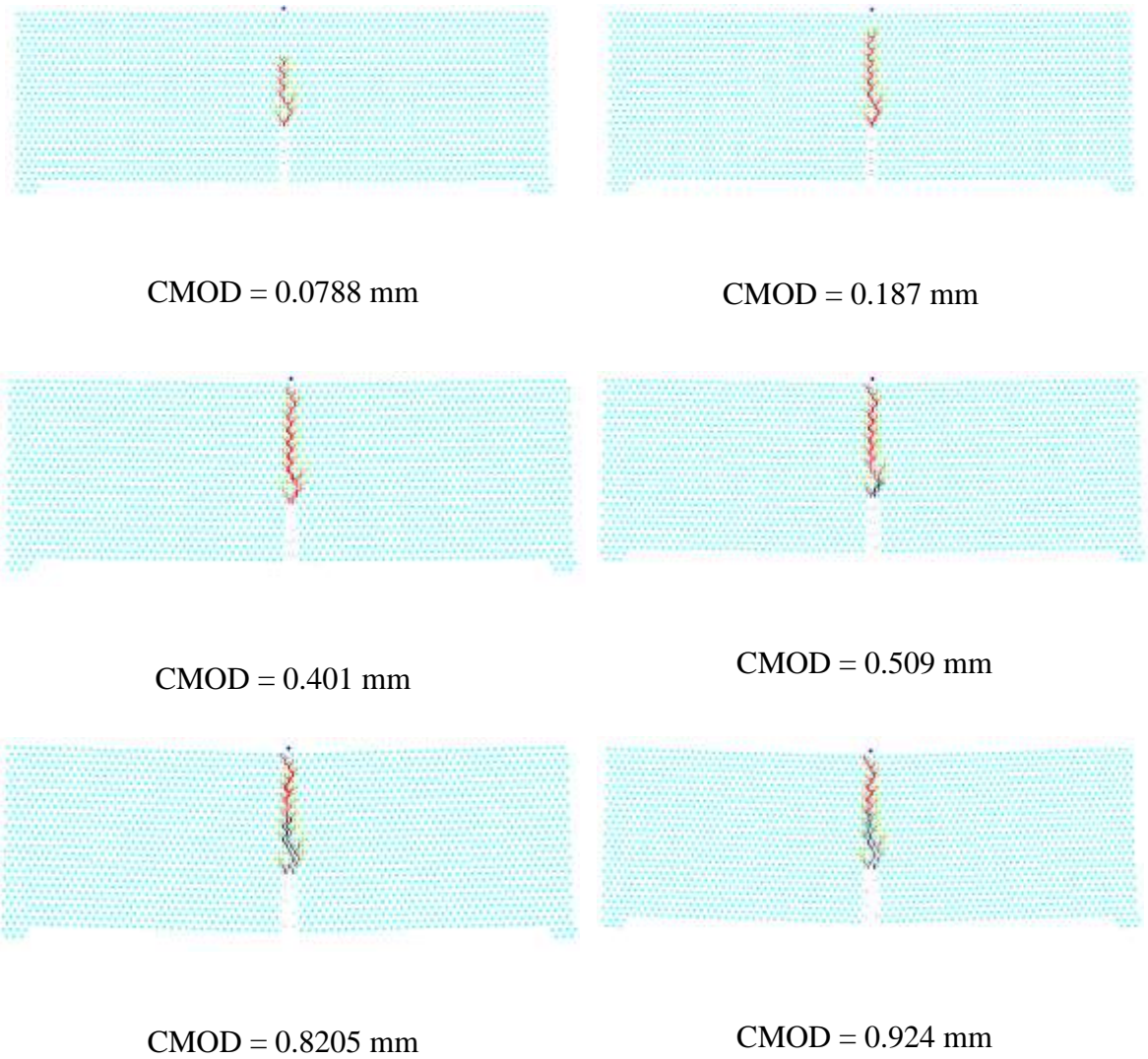


Fig. 4.14 Numerical and experimental results for CMOD-load of D9 beam, $s = 6.35$ mm



Color:	yellow	orange	brown	red
Damage index range:	0.0 to 0.3	0.3 to 0.6	0.6 to 0.8	0.8 to 1.0

Fig. 4.15 Damage pattern of D6 beam for different values of CMOD, see Fig. 4.6 for corresponding load values, $s = 6.35$ mm

4.9 Calibration of the damage model for $s = 12.70$ mm

The same strategy is used for calibrating the damage model for $s = 12.7$ mm. Since it is not possible to correctly create the geometry of D3 and D6 beams with the new last lattice spacing, the size of these beams is small to be modeled by the new lattice spacing, only D9 beam is modeled. Once again we attempted to adjust only the value of S_t for the new lattice spacing and keep the value of the other parameters fixed. Interestingly, we could successfully recalibrate the damage model with this strategy. The damage model's parameters for new lattice spacing are provided in table 4.5.

Table 4.5 The value of damage model parameters for $s = 12.7$ mm

S_t	α_1	α_2	α_3
0.00008	0.13	20.0	415

Based on the values of four damage model parameters, and assuming fixed values for α_1 , α_2 , and α_3 , the damage model is simplified to the following form:

$$\omega_t = \begin{cases} \max(0, \omega_{prev}) & \epsilon_{mp} \leq S_t \\ \max\left(1.0458\left(\frac{\epsilon_{mp} - S_t(s)}{\epsilon_{mp}}\right), \omega_{prev}\right) & S_t < \epsilon_{mp} \leq \alpha_2 S_t \\ \max\left(1 - 3.291 \times 10^{-4} \left(\frac{415 S_t(s) - \epsilon_{mp}}{\epsilon_{mp}}\right), \omega_{prev}\right) & \alpha_2 S_t < \epsilon_{mp} \leq \alpha_3 S_t \\ 1 & \epsilon_{mp} > \alpha_3 S_t \end{cases} \quad (4.2)$$

The obtained CMOD vs. load diagram, and the cracking pattern for D9 beam and $s = 12.7$ mm and are given in figures 4.16 and 4.17 respectively.

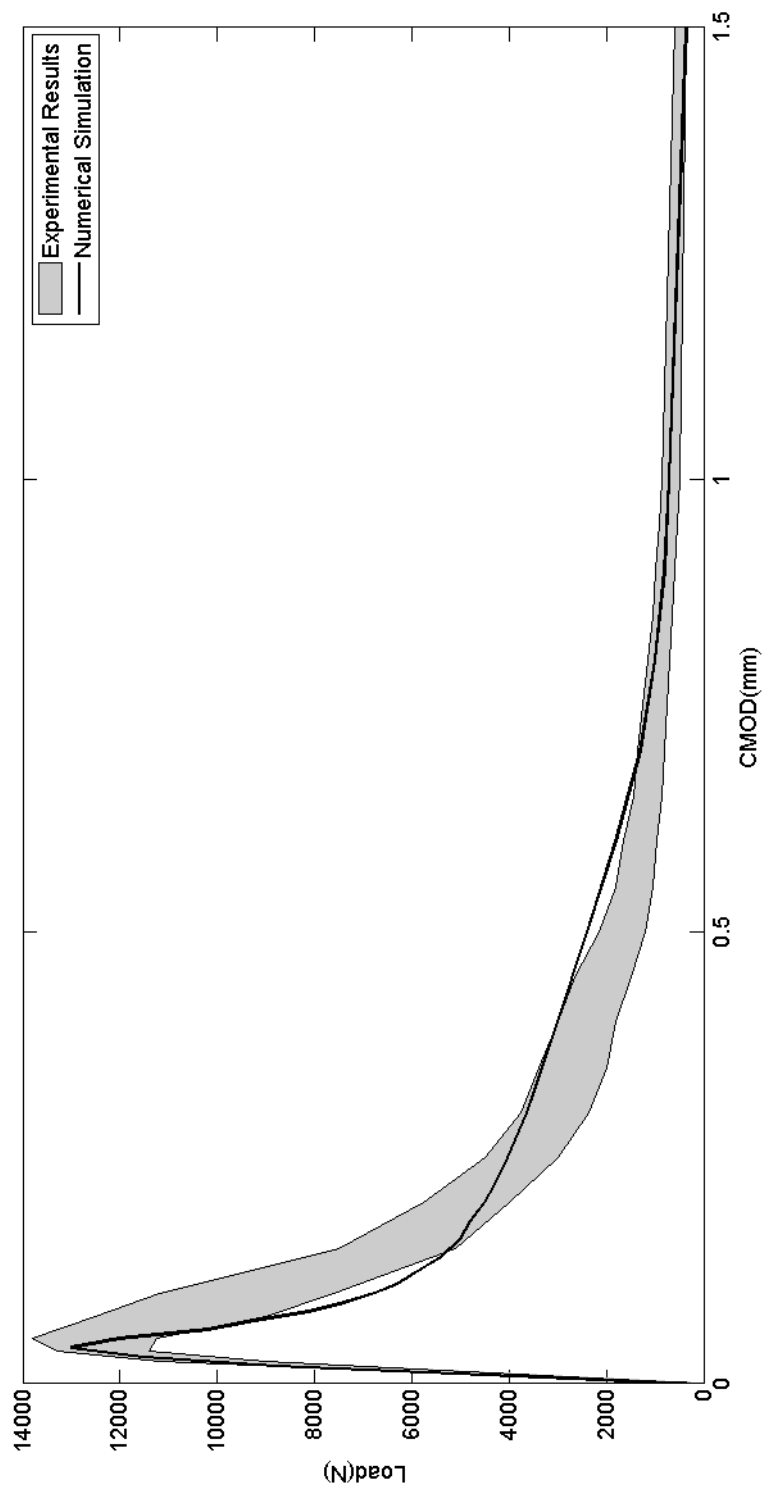
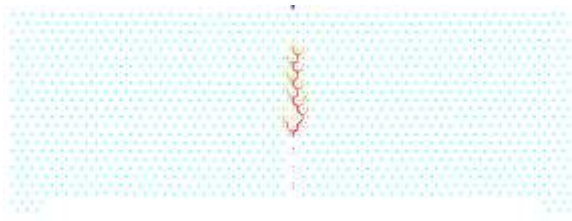
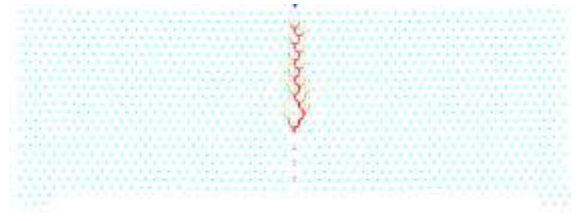


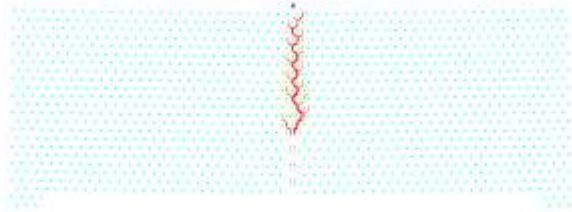
Fig. 4.16 Numerical and experimental results for CMOD-load of D9 beam, $s = 12.7$ mm



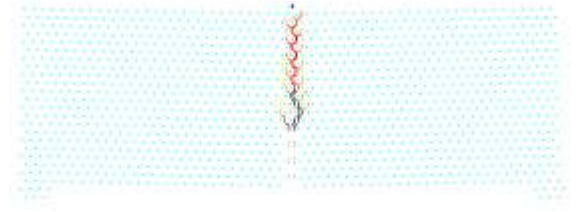
CMOD = 0.128 mm



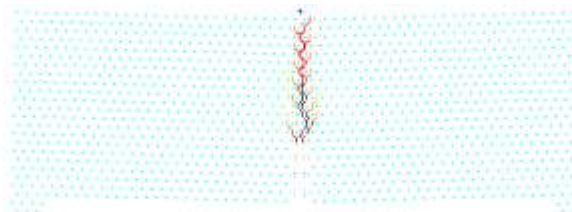
CMOD = 0.288 mm



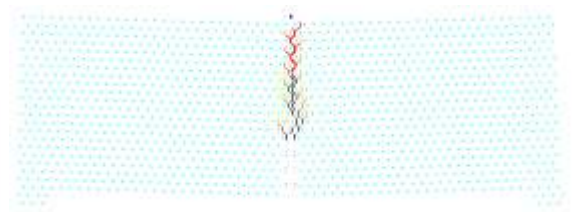
CMOD = 0.607 mm



CMOD = 0.915 mm



CMOD = 1.221 mm



CMOD = 1.376 mm

Color:	yellow	orange	brown	red
Damage index range:	0.0 to 0.3	0.3 to 0.6	0.6 to 0.8	0.8 to 1.0

Fig. 4.17 Damage pattern of D9 beam for different values of CMOD, see Fig. 4.7 for corresponding load values, $s = 12.7$ mm

Chapter 5 Conclusions

We used micropolar peridynamic lattice model to study tensile fracture of concrete. In chapter two we showed the isotropicity of the elastic hexagonal lattice. Moreover, we determined the internal forces of a the lattice under σ_{xx} , σ_{yy} , and τ_{xy} , which can be helpful in defining constitutive model for the damage in compression and interpreting the damage in shear. Furthermore, we obtained the critical time step of the explicit time integration method which is used in PDQ. We showed that twenty five percent of this number must be used as a time step in the simulations to obtain an accurate solution. We also presented the co-rotational formulation for simulation of large displacements, but small deformations.

In chapter three we introduced a new damage model. We combined axial stretch and flexural curvature of a fictitious beam to define the micropolar stretch in order to consider the role of both axial and flexural deformations in the damage of fictitious beams. Inspired by bilinear closing forces in cohesive crack models, we proposed a new damage model for micropolar peridynamics approach. The damage index is as follows:

$$\omega = \begin{cases} \max(0, \omega_{prev}) & \epsilon_{mp} \leq S_t \\ \max\left(\left(\frac{\alpha_2 - \alpha_1}{\alpha_2 - 1}\right) \frac{\epsilon_{mp} - S_t}{\epsilon_{mp}}, \omega_{prev}\right) & S_t < \epsilon_{mp} \leq \alpha_2 S_t \\ \max\left(1 - \left(\frac{\alpha_1}{\alpha_3 - \alpha_2}\right) \frac{\alpha_3 S_t - \epsilon_{mp}}{\epsilon_{mp}}, \omega_{prev}\right) & \alpha_2 S_t < \epsilon_{mp} \leq \alpha_3 S_t \\ 1 & \epsilon_{mp} > \alpha_3 S_t \end{cases}, \quad (5.1)$$

As can be seen in Eq. 5.1, this model has four unknown parameters which need to be determined. The value of these parameters were determined using inverse engineering in chapter four.

In chapter four the results of laboratory experiments which were conducted by Chapman [Chapman 2011] on three-point-bending notched beams were used to calibrate the proposed damage model. He has provided crack mouth opening displacement vs. load diagrams for three different beam sizes. In for computational loading, we carefully used the deformation control method. For this, we applied a very small amount of displacement to the particle we considered on the center top point of the beam. We also investigated and found that if the velocity applied to the particle be less than 0.08 m/s, we will eliminate dynamic effects of the loading from our simulations.

Since calibrating a model with four parameters is hard, we considered every parameter individually and studied its effect on the CMOD-load diagram, and we observed that each parameter is affecting a specific part of the diagram. We used this fact to facilitate the process of calibration. Because the damage model is mesh-dependend, the results are a function of lattice spacing, we calibrated the model for three different sizes of lattice spacing. We showed that the results of simulations are in a very good agreement with the laboratory results. Furthermore, the predicted damage and cracking pattern seemed to be very realistic. Surprisingly, the damage model is capable of distinguishing between two different approaches used in the laboratory experiments.

We also showed that three out of four parameters used to define the damage model can be assumed to be constant, at least for $3.175 \text{ mm} \leq s \leq 12.7 \text{ mm}$. The reason for this is because we defined the micropolar stretch at controlling points A and B in Fig. 3.1 in terms of S_t . Therefore, the damage model can be simplified to the following form.

$$\omega_t = \begin{cases} \max(0, \omega_{prev}) & \epsilon_{mp} \leq S_t \\ \max\left(1.0458\left(\frac{\epsilon_{mp} - S_t(s)}{\epsilon_{mp}}\right), \omega_{prev}\right) & S_t < \epsilon_{mp} \leq \alpha_2 S_t \\ \max\left(1 - 3.291 \times 10^{-4} \left(\frac{415S_t(s) - \epsilon_{mp}}{\epsilon_{mp}}\right), \omega_{prev}\right) & \alpha_2 S_t < \epsilon_{mp} \leq \alpha_3 S_t \\ 1 & \epsilon_{mp} > \alpha_3 S_t \end{cases} \quad (5.2)$$

The values of S_t for lattice spacing sizes 3.175 mm, 6.35 mm , and 12.7 mm are 0.00015, 0.000118, and 0.00008 respectively.

5.1 Future work

In my opinion, some other benchmark problems containing tensile and shear fracture are needed to be simulated to evaluate the performance of the proposed damage model, for a different loadings and specimen geometries.

References

- Arslan A. Ince R., Karihaloo B.L. (2002). “Improved Lattice Model for Concrete Fracture”, *J Eng Mech ASCE*, 128(1), 57–65.
- Bathe, K. J. (2007) “Finite Element Procedures in Engineering Analysis”, Prentice-Hall.
- Bazant, Z.P., Tabbara, M.R., Kazemi, M.T. and Pijaudier-Cabot, G. (1990). “Random Particle Model for Fracture of Aggregate or Fiber Composites”, *J. Eng. Mech. (ASCE)*, 116(8), 1686-1705.
- Bazant, Z.P. (2002). “Concrete Fracture Model: Testing and Practice”, *Eng. Fract. Mech.* 69, 165–205.
- Chapman, S. (2011), “Clarification of the Notched Beam Level II Testing Procedures of ACI 446 Committee Report 5”, Master’s Thesis, University of New Mexico, Albuquerque, NM.
- Cook, R.D, Malkus, D.S., Plesha, M.E., Witt, R.J. (1991). “Concepts and Applications of Finite Element Analysis”, John Wiley & Sons.
- Crisfield, M. A. (1991). “Non-Linear Finite Element Analysis of Solids and Structures”, Volume 1: Essentials, John Wiley & Sons.
- Gerstle, W., Sau, N., Silling, S. (2007). “Peridynamic Modeling of Concrete Structures”, *Nucl. Eng. Des.*, 237, 1250–1258.
- Gerstle, W., Honarvar Gheitanbaf, H., Asadollahi, A., Tuniki, K., Rahman, A. (2014). “Simulation of concrete using micropolar peridynamic lattice model”, Submitted to *Computational Particles Mechanics Journal*.
- Herrmann, H. J., Hansen, A., and Roux, S. (1989). “Rupture of Central Force Lattice”, *J. Phys., France*, 50(7), 733-744.
- Hillerborg A., Modeer M., Petersson P. E. (1976) “Analysis of Crack Formation and Crack Growth in Concrete by means of Fracture Mechanics and Finite Elements”. *Cement and Concrete Res.*, 6, 773–782.

- Hrennikoff, A. (1941). "Solution of Problems of Elasticity by the Framework Method", J. Appl. Mech., 8, A169-A175.
- Ince, R. (2005) "A Novel Meso-mechanical Model for Concrete Fracture", Str Eng Mech, 18(1), 28–36.
- Nguyen V. B., Chan A. H. C., Crouch R. S. (2005) "Comparisons of Smeared Crack Models for RC Bridge Pier under Cyclic Loading", 13th ACME conference, University of Sheffield, 111-114.
- Rahman, A. (2012). "Lattice-based Peridynamic Modeling of Linear Elastic Solids", Master's Thesis, University of New Mexico, Albuquerque, NM.
- Schlangen E., Van Mier J. G. M. (1992) "Simple Lattice Model for Numerical Simulation of Fracture of Concrete Materials". Materials and Structures, 25, 534–542.
- Shah, S.P, Swartz, S.E., Ouyang, C. (1995). "Fracture Mechanics of Concrete: Applications of Fracture Mechanics to Concrete, Rock and Other Quasi-Brittle Materials", Wiley, New York.
- Silling, S. A. (2000). "Reformulation of Elasticity Theory for Discontinuities and Long-Range Forces", J. Mech. Phys. Solids, 48, 175–209.